INTERNATIONAL JOURNAL FOR NUMERICAL METHODS IN FLUIDS, VOL. 8, 1403–1437 (1988)

UNSTEADY VISCOUS FLOW OVER A GROOVED WALL: A COMPARISON OF TWO NUMERICAL METHODS

S. C. HUNG* AND R. B. KINNEY

Aerospace and Mechanical Engineering Department, University of Arizona, Tucson, AZ 85721, U.S.A.

SUMMARY

A numerical study is made of the unsteady two-dimensional laminar flow of an incompressible fluid over a periodically grooved wall. Two independent finite difference techniques are employed. One is based on the vorticity–stream function and the other on the vorticity–velocity (i.e. induction law) formulation. The fluid motion is initiated impulsively from rest and is assumed to be spatially periodic in the streamwise direction. The numerical formulations are derived in detail. The generation of vorticity at the solid surface is modelled differently in the two approaches, and this is found to play an important role in determining the surface pressure distribution and the drag coefficient. The flow field is examined during the early transient phase of development, during which the greatest changes occur. Results are presented for a moderate Reynolds number (based on groove depth) equal to 100. It is found that the vorticity–stream function approach does not produce a spatially periodic wall pressure distribution, and therefore global conservation of total vorticity is not achieved. This results in substantial errors in the predictions for the drag coefficient. These deficiencies are not found in the results obtained by the vorticity–velocity formulation.

KEY WORDS Finite difference Unsteady flow Spatially periodic flows

INTRODUCTION

One is often challenged to validate a numerical study of a particular flow problem by making comparisons with experimental measurements. Unfortunately, it is rare to find experimental results in the published literature for the problem of interest and the range of parameters used. In a few instances one may find numerical results for a similar problem, and by adjusting parameters in the numerical code, the same flow problem may be reproduced. All too often, however, the available results are of a qualitative nature, and comparisons of the flow pictures are all that can be made. Many times these qualitative comparisons can be quite favourable without revealing subtle but important differences in the flow. When qualitative data are available, the comparisons are more meaningful. However, discrepancies are difficult to resolve since the exact results are not known. One must then resort to arguments about the relative merits of the approaches taken and whether or not the results seem reasonable. Such was the case in a study made by Taslim *et al.*[1] of the unsteady viscous flow generated by an impulsively rotated elliptic cylinder. Vorticity contours obtained by them were essentially the same as those obtained in an earlier study by Lugt and Ohring.[2] However, the computed moment coefficients were substantially different in magnitude. Because the two numerical formulations, and in particular the treatment of boundary conditions, were so basically different, the discrepancies in the moment predictions are still unresolved.

---

* Present address: Mechanical Engineering Department, National Chung Hsing University, Taichung, Taiwan, Republic of China.

0271–2091/88/111403–35$17.50

Received 6 February 1987
Revised 18 February 1988

In at least one instance known to the authors, a benchmark numerical solution is available for comparison purposes. This was developed by De Vahl Davis[3] for buoyancy-driven two-dimensional flows in a square cavity. It has been used by De Vahl Davis and Jones[4] to assess the accuracy of various numerical solutions to a standardized problem.

For external forced-flow problems there are no benchmark solutions in existence. However, important information can still be gathered when a single investigator compares results obtained by different methods for the same problem. This was the approach taken by Borthwick.[5] He used the vorticity–stream function (VSF) approach to compute the unsteady two-dimensional flow past a single cylinder. Two methods of representing the convective transport of vorticity were examined, and the results were found to be markedly different. Although accuracy could still not be assessed directly, incorrect trends and departures of one set of results from those previously published revealed that one of the methods was seriously in error.

In the present paper we examine two different approaches for solving the unsteady two-dimensional equations of motion for an incompressible fluid. These are based on the vorticity–stream function (VSF) and the vorticity–velocity (V–V) formulations. In the former the velocity field and wall vorticity are obtained through the stream function. The vorticity boundary condition is thus of the Dirichlet type and is applied locally. It has been used by many investigators and is considered to be the standard approach. In the V–V formulation the integral relationship (i.e. induction law) is used for the velocity calculation, and a model for the vorticity production at solid boundaries is employed which does not require a knowledge of the wall vorticity *per se*. It is rather of the Neumann type and incorporates an integral relationship (i.e. it is non-local) which involves the entire vorticity field. The model is based on a concept which was originally proposed by Lighthill[6] more than 25 years ago and which appears to have gone largely unnoticed. Because much attention has been given recently to properly posed vorticity boundary conditions, this and related work are reviewed and discussed in the next section.

The present V–V approach has been developed by Kinney and co-workers over the past 16 years for use in unsteady flow calculations. Although it has been applied only to two-dimensional problems, it can be extended to three dimensions as well. It was first applied to flows past fixed surfaces. These include a semi-infinite flat plate,[7] a finite length lifting plate[8] and an aerofoil.[9, 10] The formulation has since been generalized to include flows generated by cylinders in arbitrary unsteady motion,[1] as well as spatially periodic flows produced by arrays of cylinders.[11]

We apply the two different formulations to the prediction of the unsteady two-dimensional flow over a grooved wall. The flow is unconfined at the top, and the wall is infinitely long. In both calculations the flows are started impulsively from rest, and the solutions are advanced in time on the same computer with the same arithmetic precision. The same numerical grid, flow parameters, convective transport algorithm and time-marching scheme are used throughout. Therefore any differences which do occur may be attributed to the different numerical formulations.

The infinitely long grooved wall has advantages in that the boundary conforms to a rectangular co-ordinate system. Therefore complicated grid generation techniques are avoided. Simple periodic boundary conditions can be imposed at the inflow and outflow boundaries. In this way ambiguities are removed concerning the specification of upstream and downstream conditions. Yet this geometry produces a rich example of separated flows in which shed vortices, recirculation zones and stagnation points all develop within the flow field. Therefore it offers a demanding test of any numerical scheme.

On more practical grounds, the grooved wall is of interest because it is a model for surfaces which have been artificially roughened. This is done to enhance mixing or heat transfer rates. Some experimental studies[12, 13] have been made to see which groove geometries most economically improve heat transfer performance.

No numerical studies are known to the authors which deal with an external flow over a grooved wall. However, there are several which deal with related geometries. Gatski and Grosch[14] have studied the effect of single grooves on the drag characteristics of laminar boundary layers. Hsieh and Huang[15] have made predictions of the flow and heat transfer near single raised rectangular ribs on a smooth wall. Steady flow past a single deep groove positioned opposite a smooth wall has been studied by Ikegawa.[16] Finally, Ghaddar *et al.*[17] have investigated both steady and unsteady flows in a long channel with one smooth and one grooved wall.

VORTICITY BOUNDARY CONDITIONS

We restrict our attention to incompressible flows in two dimensions, although certainly much of the discussion applies to three dimensions as well. Also we are concerned only with the boundary conditions at solid surfaces, for it is here that all of the vorticity of the fluid is generated.

It could be argued that vorticity boundary conditions are unnatural to viscous flow problems because the viscous adherence condition only involves the velocity vector of the fluid relative to the wall, requiring it alone to vanish there. No *a priori* constraints need be imposed on the wall vorticity, and this seems justifiable since, after all, the vorticity appears in the formulation as the result of manipulating the equations of motion written in primitive variable form.

That such a view is short sighted has been effectively argued by Lighthill.[6] Those readers who are familiar with this work may wish to skip ahead to the latter part of this discussion. For the remainder, we include a summary of his viewpoints here for the sake of completeness.

Lighthill's main thesis is that vorticity is as fundamental a transport property as momentum or energy. Indeed, in two dimensions it has only one component, and its transport is governed by an equation analogous to the energy equation. Furthermore, the vorticity field determines the entire flow field, and not the reverse. That this is the case is a consequence of the velocity induction law (sometimes called the Biot–Savart law). This is an integral relationship which shows clearly that the vorticity over a significant portion of the flow affects the velocity at each and every point in the fluid and on the boundary.

In order to complete the picture, one needs to know the rate of vorticity production at solid boundaries. This is analogous to a surface heat flux in energy calculations. This production rate is non-zero whenever a pressure gradient exists along the surface, and this is usually unknown. This pressure gradient is proportional to $-\nu(\partial\omega/\partial n)_s$, where ν is the fluid kinematic viscosity, ω is the vorticity and n is the co-ordinate normal to the surface. The dimensions of this expression are acceleration and offer no insights as to the vorticity creation process *per se*. However, Lighthill clearly states that it is the vorticity production which determines the surface pressure gradient, and not the reverse. It also seems clear that Lighthill viewed the creation process as one leading to Neumann boundary conditions on the vorticity field rather than Dirichlet conditions, as commonly supposed.

Lighthill finally addresses the issue of modelling the vorticity creation process. He views the surface as being comprised of vorticity sources (and sinks), and it is only the source strengths which are in doubt. To find these, he proposes that for a given vorticity field, the velocity vector at each solid boundary point be calculated via the velocity induction law. A suitable potential flow field may need to be superimposed on the rotational velocity field in order to insure zero fluid penetration at the wall, but this does not affect the fluid vorticity. The net effect of these two fields is to produce (in general) a non-zero tangential velocity at each surface point. To enforce zero slip, a vortex sheet is supposed to exist at each point, and across this sheet the velocity changes abruptly from the slip value to the required zero value. This sheet vorticity is related to the vorticity source

strengths. To see this, suppose that the local sheet strength (it has dimensions of velocity) is determined at any instant. In the subsequent time interval (as yet unspecified) this vorticity must enter the fluid by diffusion. However, the sheet strength clearly cannot equal $-\nu(\partial\omega/\partial n)_s$, because these have different physical units. On the other hand, sheet strength divided by length does have units of vorticity, and so there must be some connection between these quantities. Unfortunately, this connection was never made by Lighthill, and he closes only with the remark that total vorticity per unit area of surface has been created and this is equal to the negative of the sheet strength. The reader is thus left with a mathematically incomplete model.

In an attempt to complete Lighthill's model,[6] Kinney and Paolino[7] investigated the unsteady flow near the leading edge of a semi-infinite flat plate. The form of the boundary condition finally adopted is given by

$$\nu \int_t^{t+\Delta t} \left.\frac{\partial \omega}{\partial n}\right|_s \mathrm{d}t' = u_{\mathrm{slip}}(s, t),$$

and has formed the basis for all of the numerical studies undertaken in References 1 and 7–11.

It can be seen that the Neumann-type boundary condition on the vorticity has been retained, but the normal derivative at the surface has been integrated over a suitable time interval Δt. This term has units of velocity, as does the right-hand side, and thus the boundary condition is dimensionally correct. It simply states that a non-zero slip velocity on a solid surface, which is found to exist at any instant of time, must equal the amount of 'total vorticity' acquired by the fluid in a subsequent time interval. Further discussion of this boundary condition plus a criterion for picking this time interval are presented in the early part of the section in which the numerical results are discussed.

The boundary condition used here allows for a precise interpretation of the vorticity creation process, and one is referred to Reference 9 for further discussion. Suffice it to say here that 'total vorticity' is the fundamental unit and has dimensions of volume/time. It is analogous to mass and thus is an extensive property, since it depends on the size of the region over which the vorticity is distributed. 'Vorticity' is total vorticity per unit volume and is the intensive property. It is analogous to density (mass per unit volume). Thus a *flux of total vorticity*, which is given by $-\nu(\partial\omega/\partial n)_s$, is analogous to mass flux (or heat flux), and we can say that *total vorticity* diffuses as a result of gradients in the *vorticity*. The flux of total vorticity is a rate expression and has dimensions of total vorticity per unit area per unit time, or simply acceleration, as previously remarked. Thus slip velocity (or vortex sheet strength) is equal to the total vorticity per unit area and is not a rate quantity.

We now turn to a discussion of other relevant works in order to relate them to the foregoing developments.

Chorin[18] has modelled the vorticity production at the surface of his cylinder in a manner reminiscent of Lighthill's approach,[6] although he seems to be unaware of this earlier work. There are many features which are interesting and novel to his analysis, but we restrict our remarks to the enforcement of vorticity boundary conditions. The slip velocity is determined at points of the surface, as previously described. Each boundary point is centred on equal length segments of the surface. The slip velocity (i.e. the total vorticity per unit area) is then multiplied by a surface area formed by this segment length multiplied by a unit depth perpendicular to the plane of the flow. Thus one has determined the total vorticity created at the surface. This is assigned to a vortex blob with a shape which is approximated by a circular area with cut-off radius σ, multiplied by a unit depth. The value of σ and the segment length of the surface are related. Once the blob is created, it is allowed to enter the fluid and migrate through it in the subsequent time evolution of the flow. Thus Chorin's model is consistent with Lighthill's. However, the former is characterized by

discrete vortices moving over a gridless field, whereas the latter treats the vorticity as being distributed over the continuous (albeit discretized) field.

Wu[19] has also given attention to vorticity boundary conditions. Many features of his analysis are similar to those already described, but one aspect is different. He supposes sheet vorticity to exist at solid surfaces, and he segments this from the remaining fluid vorticity. The fluid vorticity only is used to compute tangential (i.e. slip) velocities at points on the solid surface via the velocity induction law. The velocity field of the sheet vorticity must nullify the slip velocity, and this leads to an integral equation for the sheet vorticity. Once obtained, this sheet vorticity is converted to fluid vorticity at the wall by distributing it uniformly over a region of finite thickness (equal to one-half the distance between node points) adjacent to the surface. This value for the surface vorticity is imposed on the vorticity solution in the manner of a Dirichlet boundary condition.

Several remarks are in order here. The sheet vorticity of Wu's analysis[19] is identical to the 'bound vorticity' used in the present and earlier works by Kinney and co-workers. If the time increment used in the boundary condition of the above equation is equal to that necessary for the new total vorticity to diffuse into the incremental normal thickness taken in Wu's approach, then the seemingly different models might be expected to produce nearly identical numerical results. This does appear to be the case. However, from a theoretical point of view, this sheds no light on whether the proper boundary conditions are of the Dirichlet or Neumann type. Nevertheless, all four approaches discussed thus far do have the common feature that the boundary conditions are of the integral type and are thus global rather than local in nature.

At this point it is instructive to contrast the above treatments of vorticity boundary conditions with that which has been most commonly used in VSF formulations. In this approach the stream function ψ is prescribed at solid surfaces. Typically both ψ_s and $(\partial\psi/\partial n)_s$ are known from the imposed constraints on velocity. Suppose for the moment that a vorticity distribution exists in the fluid, and so a solution for ψ over the discrete field can be found. This solution will in general have a non-zero value of $(\partial^2\psi/\partial n^2)_s$. A Taylor series expansion through powers of Δ^2 (Δ is the spatial increment perpendicular to the wall) produces an expression for $(\partial^2\psi/\partial n^2)_s$ in terms of ψ_s, ψ_{s+1}, $(\partial\psi/\partial n)_s$ and Δ. At the wall we have a surface vorticity given by $\omega_s = -(\partial u/\partial n)_s$, which is $-(\partial^2\psi/\partial n^2)_s$. Thus values of ω_s can be generated. These boundary conditions are of the Dirichlet type and depend only on the local variations of the stream function normal to the wall. Higher-order expansions are possible, but there is a practical limit to how much of the flow region can be included in generating an expression for the wall vorticity. Wu[19] discusses further limitations of this approach.

Quartapelle and Valz-Gris[20] have devised a new approach for imposing vorticity boundary conditions in the VSF formulation. Although the mathematical treatment is somewhat involved, the basic idea is quite interesting and straightforward. A constraint is derived which involves the integral of the vorticity over the entire flow field, as well as integrals of the values of ψ_s and $(\partial\psi/\partial n)_s$ on the domain boundary. Also included in this constraint is an arbitrary harmonic function. In a practical calculation, one linearly independent harmonic function is obtained for each boundary point for which the vorticity is to be specified. Discrete values for these functions may be generated computationally over the complete flow domain by solving Laplace's equation for a unit value of the function at the boundary point in question and zero values everywhere else on the boundary. These functions need be calculated only once and stored. The vorticity transport equation is next solved using a linear decomposition scheme. One function in the solution is obtained numerically for arbitrary vorticity values prescribed at each boundary point. The linearly decomposed vorticity solution is next substituted into the integral constraint condition, along with the previously generated harmonic functions. In general the constraint condition will not be satisfied by the solution obtained for the arbitrary boundary values. However, it along with the companion

functional used in the solution decomposition must satisfy it. This allows the companion functional to be found by direct solution to a system of linear equations with number equal to the number of boundary points.

It can be seen that this scheme is computationally expensive and requires the storage of a large number of numerical solutions over the discrete field. Nevertheless, it is quite rigorous and has been used to generate a number of interesting results (see also Quartapelle[21]). A more general treatment of boundary conditions has also been made by Quartapelle and Napolitano.[22]

It is clear that in the aforementioned approach, the vorticity boundary condition at solid surfaces is taken to be of the Dirichlet type, but it is nevertheless integral in nature and is thus global. It also seems plausible that some connection exists between this and the formulations discussed earlier. If this is the case, it is likely that the connection must be made through the harmonic functions, and perhaps these can be related to the geometrical kernel functions which appear in the velocity induction law. This has yet to be done.

In a very recent work, Anderson[23] has developed a vorticity constraint which leads to explicit boundary conditions of an integral–differential nature. It is used in the VSF formulation to devise a scheme for computing the flow past a circular cylinder and a flat plate. He remarks that his numerical method is similar to that which would be obtained by Quartapelle and Valz–Gris.[20] Furthermore, it exhibits vorticity creation on the boundary which mimics that used by Chorin.[18]

As in Lighthill's and Chorin's approach, as well as that used herein and in earlier works, the velocity field is decomposed into a rotational and an irrotational part. The stream function describes the rotational velocity field and is expressed in terms of the integral over the domain of the product of a Green's function and the vorticity. The irrotational part assures that the correct normal component of velocity occurs at the boundary. In this form it is clear that the Green's function is related to the geometrical kernel function which appears in the velocity induction law. This same representation has been used previously by Panniker and Lavan.[24] It can be shown that if $G(x, y, s)$ is the Green's function, then $\partial G/\partial y$ equals the geometrical kernel function in the velocity induction law which is used in the evaluation of the x-component of the velocity. Similarly, the quantity $-\partial G/\partial x$ is equal to the kernel function used in the evaluation of the y-component of this velocity. Thus the VSF formulation becomes a V–V formulation! That such a transformation is possible has been recognized for some time.

The velocity boundary condition is next imposed, which requires that the tangential velocity at all parts of the boundary, including solid surfaces, equal the prescribed values. This boundary condition is then differentiated with respect to time and equated to zero. After several manipulations, which make use of the transport equation for vorticity and a Green's identity, a final integral–differential equation is obtained which determines the boundary values for vorticity. No attempt is made to solve this formidable equation. Rather, Anderson considers several model problems for which the analysis is easier.

Boundary layer flow over a flat plate is considered first. At this point it becomes clear that the imposed boundary condition at solid boundaries is of the Neumann type. Anderson[23] proposes a fractional time step scheme which is used to solve two unsteady equations sequentially. One is the unsteady advection equation and the other is the unsteady diffusion equation. He then isolates the vorticity created in the implementation of his boundary condition by considering its spread by diffusion only in an unsteady simulation. By assuming this newly created vorticity to be initially zero, he shows that at the end of a time step only the vorticity at the boundary is non-zero, and this is equal to $2u_{\text{slip}}/\mathrm{d}y$. That such a result can be derived is indeed remarkable. It fills in some of the details missing in Lighthill's discussion. Except for a possible minus sign, this is the vorticity associated with a sheet of strength u_{slip}, which is spread uniformly over a region of thickness $\mathrm{d}y/2$. Thus one obtains a representation which is also analogous to that used by Wu.[19] However, there

appears to be an unresolved practical issue which is not mentioned by Anderson.[23] (However, he may be aware of it. See later remarks.) This result cannot equal the fluid vorticity at the wall. To obtain this, the isolated wall vorticity must be added to that which is already present there and which was created by all events occurring earlier (see Taslim *et al.*[1]).

The remainder of Anderson's analysis[23] is devoted to consideration of the flow past a cylinder. Here he retains the stream function and applies his constraint condition locally and in differential rather than integral form. He supposes that the vorticity field is known at some time level and derives a discrete equation for a vorticity correction on the boundary. It is assumed implicitly that the boundary values of the vorticity only show up in the diffusion terms and not in the convection terms. This leads to a coupled set of linear equations for the correction vorticity at each boundary point. Once obtained, these values are then added to the values already known at the present time level. They are applied as Dirichlet boundary conditions, and the vorticity solution is advanced to a new time level. This procedure obviates the difficulty alluded to in the previous paragraph. That it produces useful numerical results is clearly demonstrated by the model cylinder problem solved. It appears to be an approach which fits in well with many already discussed.

We conclude this review with a discussion of the approach by Gazdag *et al.*[25] It is a departure from those already considered, but it has novel features worthy of consideration. They treat the flow between parallel smooth walls with periodic longitudinal end boundaries. A VSF formulation is used, and two passes are needed in their calculations. In the first, an arbitrary distribution of vorticity is assumed. Image vorticity with like signs is placed symmetrically with respect to each wall. (Note that this is in contrast to the image vorticity used in the present V–V formulation, for which the image field has opposite signs.) In this way, lateral periodicity in the stream function is also enforced, and there is zero slip velocity at the solid boundaries. This problem is solved for the stream function, and the solution will necessarily exhibit fluid penetration at the two solid walls. That is, the stream function will depart by an amount $\Delta\psi_s$ from its prescribed value. However, this penetration can be cancelled by placing boundary vorticity on the plates. The task involves finding the required boundary vorticity and then using this to correct the assumed solution. This is easily done using a technique which is reminiscent of the error vector propagation technique developed to solve the stream function equation. That technique is used in the present VSF formulation and is discussed in a later section. In essence, a unit of vorticity is placed at one boundary point, all other boundary and interior points having zero vorticity. The stream function equation is then solved, and the values obtained at each of the boundary points are saved. From these, an influence matrix can be generated, following which the corrected boundary vorticity values can be obtained as solutions to a set of linear simultaneous equations. These are added to the arbitrary values assumed at the outset to obtain corrected values. The latter are then used at boundary points, and the final solution is obtained by one more pass through the stream function equation. This correction procedure is thus somewhat similar to that used by Anderson.[23] However, this approach has a serious drawback in that an image field for vorticity must be prescribed which produces zero slip on the boundary. For the parallel plate geometry this could be obtained by inspection. It would encounter serious and perhaps insurmountable difficulties when treating general external flow problems. Nevertheless, that such a scheme is possible for this particular geometry reveals that viscous adherence conditions can be enforced through vorticity distributions which have a very diverse character.

It seems clear that a great deal of commonality, as well as diversity, exists between these various treatments of vorticity boundary conditions. It is perhaps disappointing that even in the light of such evidence, one still cannot resolve rigorously such a fundamental issue as to whether Dirichlet or Neumann boundary conditions are the correct ones. There are nevertheless strong indications that whatever the precise form may be, they must be integral in character rather than local.

Furthermore, it is the opinion of the present authors that these must involve Neumann conditions, since these occur most naturally in practice.

It is unlikely that numerical experiments will ever resolve this question, and perhaps it is not important to do so. Clearly, plausible and even excellent results can be obtained by any of the several methods discussed when used with consistent and convergent numerical formulations on good grids. For that reason, perhaps these should be classified as models for the vorticity production which occurs at solid boundaries rather than rigorous mathematical constraints or boundary conditions. In any event, we believe that some are superior to others, and we are interested here in examining two of the models discussed in this section. It is beyond the scope of this study to examine all of those reviewed here.

By way of closing, the authors recognize that impartiality is difficult to maintain when making comparative studies of this kind. Realizing this danger, care has been taken to remain unbiased. To this end, several changes have been made in the classical VSF formulation which are believed to improve the velocity and wall vorticity evaluations. These will be presented in subsequent sections.

ANALYSIS

The grooved wall is shown in Figure 1. The flow is assumed to be incompressible and spatially periodic. That is, the origin of the wall is sufficiently far upstream that the flow has reached an equilibrium state with respect to the streamwise co-ordinate. It may nevertheless vary with time. The dimension in the spanwise direction is infinite, thus helping to justify our assumption that the flow is two-dimensional.

A local Cartesian co-ordinate system has its origin at the centre of a groove. The primary computational zone has vertical boundaries at the centres of two adjacent grooves.

Governing equations

The vorticity of the fluid is governed by the vorticity transport equation, which is

$$\frac{\partial \omega}{\partial t}+\frac{\partial (u\omega)}{\partial x}+\frac{\partial (v\omega)}{\partial y}=\frac{1}{Re}\left(\frac{\partial^2 \omega}{\partial x^2}+\frac{\partial^2 \omega}{\partial y^2}\right). \tag{1}$$

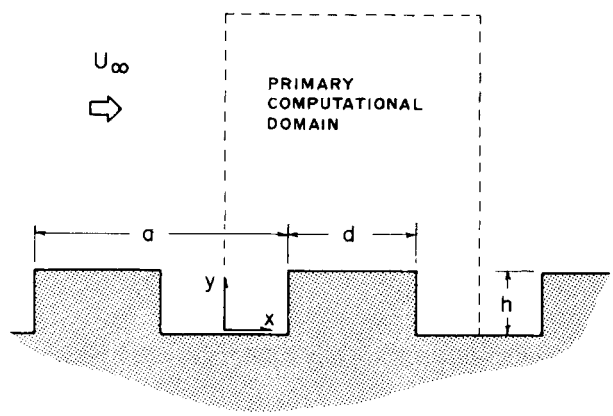

Figure 1. Schematic of flow configuration for an infinitely long grooved wall

All the variables have been rendered non-dimensional with the depth of the groove, h, the free-stream velocity U_∞ and the kinematic viscosity ν. Thus $Re = U_\infty h/\nu$. The velocity field is related to the vorticity by the relationship $\omega\mathbf{k} = \nabla \times (u\mathbf{i} + v\mathbf{j})$, where $\mathbf{i}, \mathbf{j}$ and $\mathbf{k}$ are the unit Cartesian basis vectors. In the chosen co-ordinates,

$$\frac{\partial v}{\partial x} - \frac{\partial u}{\partial y} = \omega. \tag{2}$$

Initially the fluid is at rest. Between $t = 0$ and $t = 0^+$ it is set into motion impulsively with velocity $U_\infty \mathbf{i}$. Since vorticity has not yet entered the flow field, $\omega(x, y, 0^+) = 0$ and the velocity field is irrotational at the instant following impulsive acceleration. The initial condition thus corresponds to two-dimensional potential flow. Far above the wall the velocity approaches $U_\infty \mathbf{i}$ for all time. The spatial periodicity requires that $u(0, y, t) = u(a, y, t)$ and so forth for v and ω. The boundary conditions along the wall differ for each formulation. These will be taken up subsequently.

The forces acting on the surface of the groove are of practical importance. These arise from the pressure and shear stress distributions. The shear stress can be related to the vorticity at the wall as follows:

$$\tau_w = \mu \frac{\partial u^*}{\partial n^*}\bigg|_w \left(\frac{2}{\rho U_\infty^2}\right) = -\frac{2}{Re}\omega_w. \tag{3}$$

The pressure gradient in the direction along the solid surfaces is given by

$$\frac{\partial p}{\partial s} = \nu \frac{\partial^2 u^*}{\partial n^{*2}}\bigg|_w \left(\frac{2h}{\rho U_\infty^2}\right) = -\frac{2}{Re}\frac{\partial \omega}{\partial n}\bigg|_w, \tag{4}$$

where n and s denote variables measured normal and tangential to the solid surface respectively, and the 'star' denotes a dimensional quantity. The pressure on the wall is obtained from (4) by integration. Thus

$$p_w(l) = -\frac{2}{Re}\int_0^l \frac{\partial \omega}{\partial n}\bigg|_w \mathrm{d}s. \tag{5}$$

The reference pressure $p_w(0)$ is taken to be the pressure at $x = 0$ (i.e. at the centre of the groove) and is assigned the value zero.

The drag in the direction of the onset flow is obtained by integrating the shear stress and pressure over the surface of the groove for one spatial cycle S. We obtain for the drag coefficient

$$C_D = \frac{F_D}{\frac{1}{2}\rho h U_\infty^2}$$

$$= \int_s \tau_w(\mathbf{e}_t \cdot \mathbf{i})\mathrm{d}l - \int_s p_w(\mathbf{e}_n \cdot \mathbf{i})\,\mathrm{d}l \tag{6}$$

$$= -\frac{2}{Re}\left[\int_s \left(\omega_w(\mathbf{e}_t \cdot \mathbf{i}) - \int_0^l \frac{\partial \omega}{\partial n}\bigg|_w (\mathbf{e}_n \cdot \mathbf{i})\mathrm{d}s\right)\mathrm{d}l\right]. \tag{7}$$

The unit vector $\mathbf{e}_n$ is the outward drawn normal. The manner in which ω_w and $(\partial\omega/\partial n)_w$ are expressed in terms of the flow variables depends on the formulation used. This will be taken up in the next sections.

Vorticity–stream function formulation

The stream function is introduced such that $u=\partial\psi/\partial y$ and $v=-\partial\psi/\partial x$, from which

$$\frac{\partial^2\psi}{\partial x^2}+\frac{\partial^2\psi}{\partial y^2}=-\omega. \tag{8}$$

Far above the wall we have $(\partial\psi/\partial y)_{y\to\infty}=1{\cdot}0$. At the wall the no-slip condition must be enforced. The zero-penetration condition gives $\psi_w=0$. A zero slip velocity is enforced through the circulation theorem. Thus for finite values of ε and δ, we have approximately

$$-\omega(x,\varepsilon/2,t)\,\varepsilon\,\delta\simeq v(x-\delta/2,\varepsilon/2,t)\varepsilon+u(x,\varepsilon,t)\delta-v(x+\delta/2,\varepsilon/2,t)\varepsilon. \tag{9}$$

The foregoing result is obtained by applying Stoke's theorem to a region of height ε and horizontal extent δ. The vorticity and velocity terms are evaluated centrally, and the tangential velocity at the wall, $u(x,0,t)$, has been set equal to zero.

As a first approximation, the vertical velocity terms in (9) can be neglected and $\omega_w\simeq\omega(x,\varepsilon/2,t)$. Thus $\omega_w\simeq-u(x,\varepsilon,t)/\varepsilon$. This is an approximate expression for the vorticity of the fluid at the wall. If one writes $u(x,\varepsilon,t)\simeq\psi(x,\Delta,t)/\Delta$, where $\Delta=2\varepsilon$, then one has $\omega_w(x,\varepsilon/2,t)\simeq-2\psi(x,\Delta,t)/\Delta^2$. This is a familiar equation which is accurate to $O(\Delta)$ and was deduced as early as 1928. The usual derivation is based on a Taylor's series expansion of the stream function. This is the expression for wall vorticity which is used most frequently in VSF formulations. Roache[26] (p. 141) discusses this and higher-order schemes.

In this work a slight departure is taken from the usual approach, and the wall vorticity is evaluated directly from equation (9). The vertical velocity terms are not neglected and are expressed in terms of the stream function. The final result will be given when the numerical formulation is discussed. Once the wall vorticity is found from (9) it is imposed on the solution to equation (1) at each point on the grooved wall. This boundary condition is thus of the Dirichlet type.

Vorticity–velocity formulation

The formulation involving the velocity induction law is a bit more involved than that previously described. We begin by writing the solution to equation (2). This equation is nothing more than that given by $\boldsymbol{\omega}=\mathrm{curl}\,\mathbf{V}$. The solution[27] is well known and is given in two dimensions by

$$\mathbf{V}^*(r_p^*,t^*)=\mathbf{V}_\infty^*+\frac{1}{2\pi}\int\!\!\int_A\frac{\omega_o^*\times\mathbf{r}_{op}^*}{|\mathbf{r}_{op}^*|^2}\,\mathrm{d}A^*+\mathrm{grad}\,\phi. \tag{10}$$

The term $\mathrm{grad}\,\phi$ is a purely irrotational contribution to the velocity field. It is added here for complete generality and to help satisfy boundary conditions.

In the application of (10), we replace $\mathrm{grad}\,\phi$ by a suitable distribution of 'bound' vorticity γ over the surface of the grooved wall. The 'free' vorticity ω is in the fluid, and both vorticity distributions have an image field (equal in strength but opposite in sense of rotation) in the lower half-plane.

It is convenient to envision that a 'step' separates two adjacent grooves, as shown in Figure 1. When the image field is considered, there is flow symmetry about the plane coincident with the bottom of the grooves. Thus fluid cannot penetrate these surfaces. Accordingly, bound vorticity is needed only on the three surfaces comprising the step and not on the bottoms of the grooves.

We thus write

$$\mathrm{grad}\,\phi\equiv\frac{1}{2\pi}\int_\Gamma\frac{\gamma_q^*\times\mathbf{r}_{qp}^*}{|\mathbf{r}_{qp}^*|^2}\mathrm{d}l^*. \tag{11}$$

To insure that there is zero penetration on the surface of the step, γ must be especially distributed, and this leads to an integral equation governing γ. This will be discussed later.

The ranges of integration A and Γ must include all non-zero vorticity. Since the flow field is spatially periodic, we can write $\omega^*(x, y, t)=\omega^*(x+na, y, t)$ and so forth for γ. This follows the scheme used by Cerutti *et al.*,[11] except that in the present problem there is no staggered antisymmetry. Details of the derivation are given in the dissertation[28] on which this paper is based. One then obtains integrals over the regions corresponding to $n=0, \pm 1, \pm 2$, etc., extending to $n=\pm\infty$.

The final result can be expressed in terms of integrals only over the primary computational domain given by $n=0$. We thus can write for the two non-dimensional velocity components

$$u_p=1-\frac{1}{2a}\iint_A \omega_o[K_{\mathrm{I}}(x_o, x_p, y_o, y_p)-K_{\mathrm{I}}(x_o, x_p, -y_o, y_p)]\,\mathrm{d}x_o\,\mathrm{d}y_o$$

$$-\frac{1}{2a}\int_\Gamma \gamma_q[K_{\mathrm{I}}(x_q, x_p, y_q, y_p)-K_{\mathrm{I}}(x_q, x_p, -y_q, y_p)]\mathrm{d}l_q, \tag{12}$$

$$v_p=\frac{1}{2a}\iint_A \omega_o[K_{\mathrm{II}}(x_o, x_p, y_o, y_p)-K_{\mathrm{II}}(x_o, x_p, -y_o, y_p)]\,\mathrm{d}x_o\,\mathrm{d}y_o$$

$$+\frac{1}{2a}\int_\Gamma \gamma_q[K_{\mathrm{II}}(x_q, x_p, y_q, y_p)-K_{\mathrm{II}}(x_q, x_p, -y_q, y_p)]\mathrm{d}l_q, \tag{13}$$

where

$$K_{\mathrm{I}}(x_1, x_2, y_1, y_2)=\frac{\sinh[2\pi(y_2-y_1)/a]}{\cosh[2\pi(y_2-y_1)/a]-\cos[2\pi(x_2-x_1)/a]}, \tag{14}$$

$$K_{\mathrm{II}}(x_1, x_2, y_1, y_2)=\frac{\sin[2\pi(x_2-x_1)/a]}{\cosh[2\pi(y_2-y_1)/a]-\cos[2\pi(x_2-x_1)/a]}. \tag{15}$$

When one considers the upper and lower half-planes together, it is interesting to note that the velocity field given by the foregoing equations corresponds to that in a viscous fluid flowing past a single in-line row of rectangular cylinders, the centres of which are rigidly joined by plates of infinitesimal thickness. We are, however, only interested in the characteristics of the flow in the upper half-plane.

The integral equation for γ can be obtained from equations (12) and (13) by setting the tangential velocities to zero at a distance ε interior to step surfaces. Along the top of the step we apply (12). The left-hand side is set equal to zero and $y_p=h-\varepsilon$. The independent variable is x_p, and it ranges from $(a-d)/2+\varepsilon$ to $(a+d)/2-\varepsilon$. The governing equation is

$$\frac{1}{2a}\int_\Gamma \gamma_q[K_{\mathrm{I}}(x_q, x_p, y_q, y_p)-K_{\mathrm{I}}(x_q, x_p, -y_q, y_p)]\mathrm{d}l_q$$

$$=1-\frac{1}{2a}\iint_A \omega_o[K_{\mathrm{I}}(x_o, x_p, y_o, y_p)-K_{\mathrm{I}}(x_o, x_p, -y_o, y_p)]\,\mathrm{d}x_o\,\mathrm{d}y_o. \tag{16a}$$

Along the front and back vertical surfaces of the step we apply (13) with the left-hand side equal to zero. The variable x_p is either $(a-d)/2+\varepsilon$ or $(a+d)/2-\varepsilon$, and y_p ranges from zero to $h-\varepsilon$. The

governing equation is

$$\frac{1}{2a}\int_\Gamma \gamma_q[K_{II}[x_q, x_p, y_q, y_p) - K_{II}(x_q, x_p, -y_q, y_p)]\mathrm{d}l_q$$
$$= -\frac{1}{2a}\iint_A \omega_o[K_{II}(x_o, x_p, y_o, y_p) - K_{II}(x_o, x_p, -y_o, y_p)]\,\mathrm{d}x_o\,\mathrm{d}y_o. \tag{16b}$$

In the foregoing, $\mathrm{d}l_q$ is defined as follows:

$$\mathrm{d}l_q = \begin{cases} \mathrm{d}x_q, & \text{if } \gamma_q \text{ is located at the horizontal surface of the step,} \\ \mathrm{d}y_q, & \text{if } \gamma_q \text{ is located at the vertical surface of the step.} \end{cases}$$

In the above integral equations the range of integration is over the three surfaces of the step. The entire right-hand side of equation (16), which includes the integral involving ω_o, constitutes a non-homogeneous (but nevertheless known) term at each of the points defined by the independent variables (x_p, y_p). Although explicit equations could be written down as $\varepsilon \to 0$, this is not useful since they will ultimately be solved in discrete form, as described later.

As a final note, we emphasize that the steps used in obtaining the integral equation for γ involved setting the tangential velocity to zero just interior to the surfaces of the step. This produces a Fredholm equation of the second kind. Had we required that the normal velocity component vanish, an equation of the first kind would have been produced. The equation of the second kind is easier to solve numerically since it leads to diagonal dominance in the system of linear simultaneous equations derived from it. In any event, the normal velocity component is effectively cancelled with either approach. This follows since the velocity field inside the step must still be irrotational, and it is in fact identically zero if either velocity component vanishes. It is also observed that the governing integral equation for γ admits a complementary solution corresponding to the case where the non-homogeneous term of equation (16) is absent. This corresponds to pure circulatory flow about the square cylinder. Such a flow would penetrate the bottom of the groove and is excluded by the image system imposed on the distribution for γ. Therefore this complementary solution is identically zero for the case treated here.

It remains to specify the boundary conditions at the solid wall. It is easily verified that the transverse component of velocity given by equation (13) vanishes when $y_p = 0$. Furthermore, the bound vorticity is so distributed that there is no fluid penetration at the three surfaces of the step. Nevertheless, there may be a non-zero tangential component of velocity on the solid surfaces just interior to the fluid. As originally stated by Lighthill,[6] such a slip velocity must be cancelled by a generation of free vorticity.

On the left vertical face and top surfaces of the step the tangential slip velocity is equal to $-\gamma$. On the right vertical surface the slip velocity is equal to $+\gamma$. On the bottom of the groove the slip velocity is given by equation (12) with $y_p = 0$. Therefore the slip velocity is considered to be known at each point of the solid boundary and at each time level. Call this slip velocity $U_{\text{slip}}(s, t)$. According to the vorticity production model employed here, we write

$$\frac{1}{Re}\int_t^{t+\Delta t} \left.\frac{\partial \omega}{\partial n}\right|_{\text{wall}} \mathrm{d}t' = \pm U_{\text{slip}}(s, t), \tag{17}$$

where Δt must be chosen according to a criterion which is given in the early part of the section in which the numerical results are presented and discussed. The ambiguous sign depends on the location of the point s. For a positive slip velocity on the bottom of the groove and the left vertical face and top of the step, negative (i.e. clockwise) free vorticity is produced. Therefore $\partial\omega/\partial n$ at the wall is positive and the positive ambiguous sign is used. On the other hand, a positive (i.e. upward

directed) slip velocity on the right vertical face produces positive free vorticity. Thus $\partial\omega/\partial n$ is negative at the wall and the negative ambiguous sign is used.

Equation (17) is the form of the boundary condition to be imposed on the solution to equation (1). It is of the Neumann type and differs fundamentally from that used in the stream function formulation and given by equation (9). Furthermore, the condition given by (17) most directly relates to the evaluation of the pressure distribution on the surface, as seen from (4) and (5). On the other hand, the wall vorticity obtained from (9) leads to a direct determination of the shear stress distribution from equation (3). Thus it can be anticipated that the drag predictions obtained by the two approaches may differ depending on which of the surface force contributions dominate.

NUMERICAL METHODS

The computational grid is shown in Figure 2. We have selected a fixed geometry with $a=4{\cdot}0$ and $d=2{\cdot}0$. The grid lines correspond to boundaries of control volumes, at the centres of which are placed node points. There are no node points on the grooved wall.

The grid spacing near the corners of the step was obtained using an algorithm based on the Schwarz–Christoffel transformation for the potential flow in a channel with a single forward facing step which is infinitely long in the flow direction. The height of the step was chosen to be $1-(0{\cdot}9)^{1/2}$ times the distance between the channel walls upstream of the step. The height of the step in the transformed plane was divided into ten uniform spatial increments, and the corresponding increments in the physical plane were obtained. The first seven of these are as

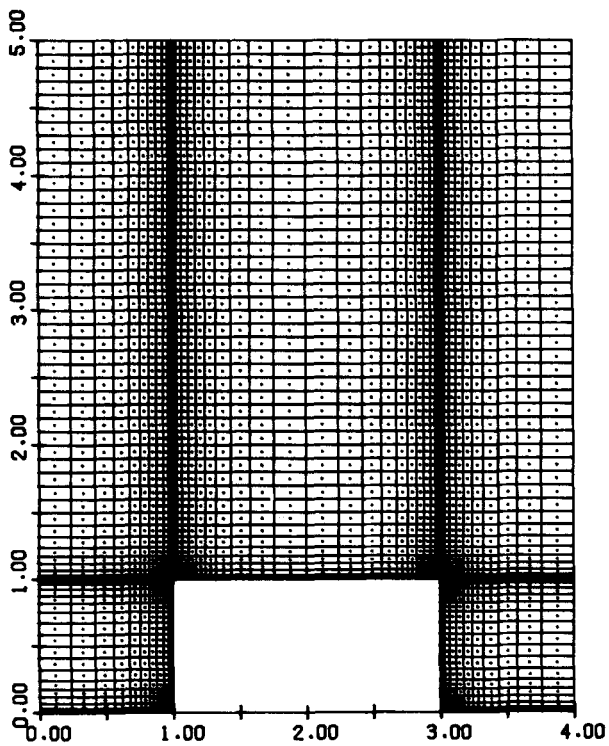

Figure 2. Grid network used in the numerical calculations

follows: 0·00893428, 0·0223357, 0·0376768, 0·0498574, 0·0553687, 0·0687468 and 0·0800158. These were chosen as base increments and their sum equals 0·3229355. This sum was subtracted from 0·5 and the difference was divided by 2·0. These two equal increments plus the seven base increments produce the grid arrangement from $y=0{\cdot}5$ to 1·0 in Figure 2. It is reflected to produce the spacing from $y=0$ to 0·5 and from $y=1{\cdot}0$ to 1·5. For $y \geqslant 1{\cdot}5$ the spacing is uniform and equal to 0·10.

The horizontal spacing between $x=1{\cdot}0$ and 2·0 uses these same seven base increments plus the four increments given by 0·114167, 0·144114, 0·179479 and 0·239305. This is then reflected to produce the spacing over the rest of the step and the bottom of the groove.

The vorticity transport equation is first integrated over a rectangular control volume $\Delta x_i \Delta y_j$ as shown in Figure 3. The exact result is

$$\frac{\partial}{\partial t}\iint \omega \,dx\,dy = -\iint \mathrm{div}(\mathbf{i}u\omega + \mathbf{j}v\omega)\,dx\,dy + \frac{1}{Re}\iint \mathrm{div}(\mathrm{grad}\,\omega)\,dx\,dy. \tag{18}$$

By the divergence theorem we can write

$$\iint \mathrm{div}(\mathbf{i}u\omega + \mathbf{j}v\omega)\,dx\,dy = \int_{y_{j-1/2}}^{y_{j+1/2}} [(-u\omega)_{x_{i-1/2}} + (u\omega)_{x_{i+1/2}}]\,dy + \int_{x_{i-1/2}}^{x_{i+1/2}} [(-v\omega)_{y_{j-1/2}} + (v\omega)_{y_{j+1/2}}]\,dx \tag{19}$$

and

$$\iint \mathrm{div}(\mathrm{grad}\,\omega)\,dx\,dy = \int_{y_{j-1/2}}^{y_{j+1/2}} \left[-\left(\frac{\partial \omega}{\partial x}\right)_{x_{i-1/2}} + \left(\frac{\partial \omega}{\partial x}\right)_{x_{i+1/2}}\right] dy + \int_{x_{i-1/2}}^{x_{i+1/2}} \left[-\left(\frac{\partial \omega}{\partial y}\right)_{y_{j-1/2}} + \left(\frac{\partial \omega}{\partial y}\right)_{y_{j+1/2}}\right] dx. \tag{20}$$

The representative transport terms for a control volume centred on node (i,j) are now

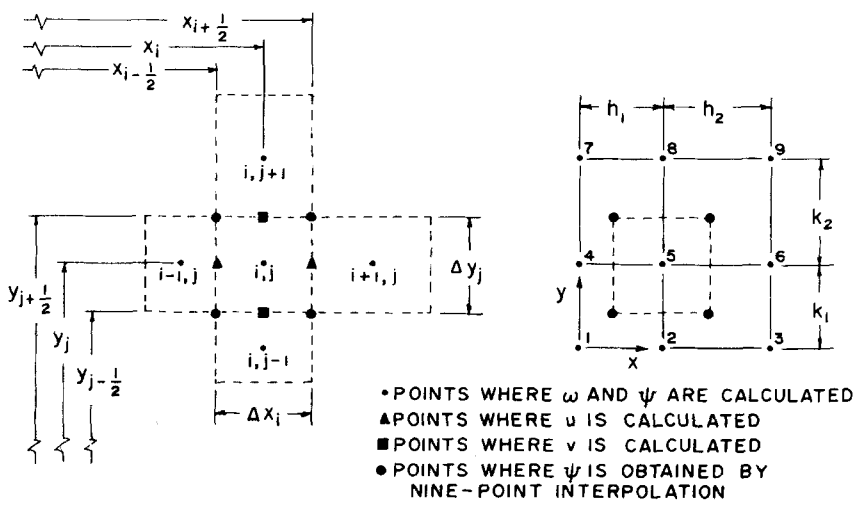

Figure 3. Schematic of fluid cell and node arrangement used to evaluate the flow variables

approximated as follows:

$$\int_{y_{j-1/2}}^{y_{j+1/2}} \left(\frac{\partial \omega}{\partial x}\right)_{x_{i+1/2}} \mathrm{d}y \simeq \left(\frac{\omega_{i+1,j}-\omega_{i,j}}{0{\cdot}5(\Delta x_i+\Delta x_{i+1})}\right)\Delta y_j, \tag{21}$$

$$\int_{y_{j-1/2}}^{y_{j+1/2}} (u\omega)_{x_{i+1/2}} \mathrm{d}y \simeq (u_{i+1/2,j}\,\omega_{i,j})\Delta y_j. \tag{22}$$

Note that the convective velocity u (assumed to be positive) convects vorticity assigned to the upwind node. If u turns out to be negative, then the vorticity in (22) is assigned the value ω_{i+1}. The same upwinding scheme is used for the transverse convection.

The storage term is approximated by

$$\frac{\partial}{\partial t}\int\int \omega \mathrm{d}x\mathrm{d}y \simeq \left(\frac{\partial}{\partial t}\omega_{i,j}\right)\Delta x_i \Delta y_j \tag{23}$$

and it remains to do a final integration with respect to time. For this we use the explicit (Euler) time method. If k denotes the time index, i.e. $t=k\Delta t$, $t+\Delta t=(k+1)\Delta t$, then equation (23) integrates exactly to give $(\omega_{i,j}^{k+1}-\omega_{i,j}^{k})\Delta x_i \Delta y_j$. The integration of the terms on the right-hand side of equation (20) gives, for example,

$$\int_t^{t+\Delta t}\left[\int_{y_{j-1/2}}^{y_{j+1/2}} \left(\frac{\partial \omega}{\partial x}\right)_{x_{i+1/2}} \mathrm{d}y\right]\mathrm{d}t' \cong \left(\frac{\omega_{i+1,j}^{k}-\omega_{i,j}^{k}}{0{\cdot}5(\Delta x_i+\Delta x_{i+1})}\right)\Delta y_j \Delta t, \tag{24}$$

and so on and so forth. When all terms are introduced into the governing equation, one obtains for an interior node

$$\begin{aligned}
\omega_{i,j}^{k+1} = \omega_{i,j}^{k}\Bigg\{ & 1-u_{i+1/2,j}^{k}\frac{\Delta t}{\Delta x_i}-v_{i,j+1/2}^{k}\frac{\Delta t}{\Delta y_j} \\
& -\frac{2\Delta t}{Re}\Bigg[\frac{1}{\Delta x_i}\left(\frac{1}{\Delta x_i+\Delta x_{i+1}}+\frac{1}{\Delta x_i+\Delta x_{i-1}}\right) \\
& +\frac{1}{\Delta y_j}\left(\frac{1}{\Delta y_j+\Delta y_{j+1}}+\frac{1}{\Delta y_j+\Delta y_{j-1}}\right)\Bigg]\Bigg\} \\
& +\omega_{i+1,j}^{k}\left(\frac{2\Delta t/Re}{\Delta x_i(\Delta x_i+\Delta x_{i+1})}\right)+\omega_{i-1,j}^{k}\left(\frac{u_{i-1/2,j}^{k}}{\Delta x_i}+\frac{2/Re}{\Delta x_i(\Delta x_i+\Delta x_{i-1})}\right)\Delta t \\
& +\omega_{i,j+1}^{k}\left(\frac{2\Delta t/Re}{\Delta y_j(\Delta y_j+\Delta y_{j+1})}\right)+\omega_{i,j-1}^{k}\left(\frac{v_{i,j-1/2}^{k}}{\Delta y_j}+\frac{2/Re}{\Delta y_j/(\Delta y_j+\Delta y_{j-1})}\right)\Delta t.
\end{aligned} \tag{25}$$

Attention is drawn to the fact that the convective velocities are evaluated at central points on the vertical and horizontal control faces, as shown by the triangular and square symbols in Figure 3. The manner in which these are evaluated depends on the particular formulation used. This plus the implementation of boundary conditions are taken up in the next sections.

This scheme for solving the vorticity transport equation can be classified as forward in time and centred in space (FTCS) as far as the unsteady and diffusion terms are concerned. It uses the second-upwinding difference scheme discussed by Roache[26] (p. 73) for the convective terms. A great deal is known about this finite difference formulation as regards the stability requirements on the time step. That it also exhibits artificial (i.e. numerical) diffusion is also well known.

Recent papers by Gresho and co-workers[29-31] have considered these matters in some detail. Although rigorous results can be obtained only for the model advection–diffusion equation (i.e.

flow with uniform velocity) solved on a uniform grid, some insights are provided for the vorticity equation used here and given by equation (25).

A heuristic argument for stability shows that Δt must be chosen such that the term in curly brackets, which multiplies $\omega_{i,j}^k$ on the right-hand side of equation (25), is greater than or equal to zero. This is also true for the counterparts of (25), which must apply adjacent to the boundaries of the computational domain. On a uniform mesh with constant velocity components, this reduces to the stability requirement given in Reference 29. Since the present formulation involves the unknown convective velocities at each time level, the choice of Δt has to be made as the solution progresses. The range of values used in the present study is given in the section in which the results are discussed.

Concerning the numerical diffusion, it is known that the upwinding does increase the effective fluid diffusivity, whereas the Euler explicit time-differencing scheme decreases it. In regions of low velocity, such as recirculation zones of the flow, these effects are small on fine grids. In other regions where streamwise diffusion and cross-stream convection are small (i.e. where boundary layer approximations are valid), numerical diffusion can also be expected to be unimportant. These fortuitous circumstances may explain in part the success that this scheme has had in a large number of numerical simulations. Most importantly, however, it is reasoned that the outcome of the present comparison study is not influenced by the presence of numerical diffusion in the vorticity solution. This is because it appears in equal amounts in each formulation.

Vorticity–stream function formulation

If we apply the circulation theorem to a cell element $\Delta x_i \Delta y_j$ in the fluid, the numerical analogue of equation (8) is obtained as follows:

$$-\omega_{i,j}\Delta x_i \Delta y_j = \frac{\psi_{i,j+1}-\psi_{i,j}}{0{\cdot}5(\Delta y_j+\Delta y_{j+1})}\Delta x_i - \frac{\psi_{i,j}-\psi_{i+1,j}}{0{\cdot}5(\Delta x_i+\Delta x_{i+1})}\Delta y_j$$
$$-\frac{\psi_{i,j}-\psi_{i,j-1}}{0{\cdot}5(\Delta y_{j-1}+\Delta y_j)}\Delta x_i + \frac{\psi_{i-1,j}-\psi_{i,j}}{0{\cdot}5(\Delta x_{i-1}+\Delta x_i)}\Delta y_j, \tag{26}$$

where it is important to remember that the velocities that make up the right-hand side of (26) are tangential to the surfaces of the cell element. Upon simplification, one has the final equation

$$\psi_{i,j-1} = B\omega_{i,j} + C\psi_{i,j} + D\psi_{i,j+1} + E\psi_{i+1,j} + F\psi_{i-1,j}, \tag{27a}$$

where

$$B = -\frac{\Delta y_j(\Delta y_{j-1}+\Delta y_j)}{2}, \tag{27b}$$

$$C = 1 + \frac{\Delta y_j(\Delta y_{j-1}+\Delta y_j)}{\Delta x_i(\Delta x_i+\Delta x_{i+1})} + \frac{\Delta y_j(\Delta y_{j-1}+\Delta y_j)}{\Delta x_i(\Delta x_i+\Delta x_{i-1})} + \frac{\Delta y_{j-1}+\Delta y_j}{\Delta y_j+\Delta y_{j+1}}, \tag{27c}$$

$$D = -(\Delta y_{j-1}+\Delta y_j)/(\Delta y_j+\Delta y_{j+1}), \tag{27d}$$

$$E = -\Delta y_j(\Delta y_{j-1}+\Delta y_j)/\Delta x_i(\Delta x_i+\Delta x_{i+1}), \tag{27e}$$

$$F = -\Delta y_j(\Delta y_{j-1}+\Delta y_j)/\Delta x_i(\Delta x_i+\Delta x_{i-1}). \tag{27f}$$

Recall that the far field boundary condition is given by $(\partial\psi/\partial y)|_{y\to\infty} = 1{\cdot}0$. Since the computational domain must be finite, this condition is assumed to be satisfied when $y > 4{\cdot}9$. If the central difference formula is employed for $\partial\psi/\partial y$, one obtains for the stream function along the top row of

nodes

$$\psi_{i,N}=\psi_{i,N-1}+(\Delta y_N+\Delta y_{N-1})/2. \tag{28}$$

On the other hand, if ψ at the interior node points along the left and right vertical boundaries is denoted as $\psi_{2,j}$ and $\psi_{M,j}$, respectively, the periodic boundary condition then becomes

$$\psi_{1,j}=\psi_{M,j}, \tag{29a}$$

$$\psi_{M+1,j}=\psi_{2,j}. \tag{29b}$$

Finally, we consider the treatment of the boundary condition at the bottom solid surface. Along this surface ψ must be zero. However, the numerical scheme used to obtain the stream function requires the calculation of ψ at this surface. As a result, this wall condition becomes the controlling criterion in the determination of ψ for the entire field. To obtain the finite difference expression for $\psi_{i,w}$, we first consider a control volume surrounding the point (i,j) just above the wall. The height of this control volume is $0{\cdot}75\Delta y_j$, and the lower control face is midway between the wall and node (i,j). Using the same procedure as used to derive equation (27), we obtain

$$\begin{aligned}\psi_{i,w}=&-(0{\cdot}375\Delta y_j^2)\omega_{i,j}+\left[1+\frac{\Delta y_j}{\Delta y_j+\Delta y_{j+1}}+0{\cdot}75\Delta y_j^2\left(\frac{1}{\Delta x_i(\Delta x_i+\Delta x_{i+1})}\right.\right.\\&\left.\left.+\frac{1}{\Delta x_i(\Delta x_i+\Delta x_{i-1})}\right)\right]\psi_{i,j}-\left(\frac{0{\cdot}75\Delta y_j^2}{\Delta x_i(\Delta x_i+\Delta x_{i+1})}\right)\psi_{i+1,j}\\&-\left(\frac{0{\cdot}75\Delta y_j^2}{\Delta x_i(\Delta x_i+\Delta x_{i-1})}\right)\psi_{i-1,j}-\left(\frac{\Delta y_j}{\Delta y_j+\Delta y_{j+1}}\right)\psi_{i,j+1}.\end{aligned} \tag{30}$$

A similar expression is obtained if the control volume is adjacent to a vertical surface of the groove. Note that this equation does not require a knowledge of the wall vorticity. Its evaluation will be taken up subsequently.

The solution algorithm used to calculate ψ is based on the stabilized error vector propagation (SEVP) method as described by Madala and McDonald.[32] It is a direct (i.e. non-iterative) method and is an extension of the error vector propagation (EVP) method described by Roache.[26]

In the calculation, we begin at the second row from the top (i.e. $j=N-1$) of the computational domain. If values for the stream function along this row of nodes are assigned arbitrarily, the value of ψ for the nodes at the top boundary (i.e. $j=N$), the left boundary (i.e. $i=1$) and the right boundary (i.e. $i=M+1$) can then be obtained using equations (28) and (29a, b). Following this, equation (27) can be used to obtain ψ at the next lower row of nodes (i.e. $j=N-2$). The result is an expression for $\psi_{i,N-2}$ in terms of $\psi_{i-1,N-1}, \psi_{i,N-1}, \psi_{i+1,N-1}, \psi_{i,N}$, where $i=2, 3, \ldots, M$, and the free vorticity $\omega_{i,j}$. This procedure is repeated for the next lower row of nodes (i.e. $j=N-3$, $N-4, \ldots$) until the nodes are reached at the solid surfaces. The stream function there is calculated by (30) and its counterpart for the vertical solid surfaces. Had the initial distribution for ψ along $j=N-1$ been correctly given, then $\psi_{i,w}$ would be zero as required. The departure of $\psi_{i,w}$ from zero is a measure of the error, and one can correct the guess for ψ along the second row of nodes from the top according to a systematic procedure. In this way the correct distribution at $j=N-1$ can be deduced and the true values for the stream function over the entire field can be determined. As stated earlier, this is a direct solution method which avoids iteration. It has been used in a recent study[33] of large-eddy break-up by a plate imbedded in a boundary layer.

This method fails when the number of computational cell elements in the marching direction (i.e. the downward vertical direction) is large. This is because the error introduced at the second row of nodes from the top will eventually grow until the solution is meaningless. Therefore the

solution has to be stabilized by subdividing the vertical extent of the domain into subregions or blocks. A direct measure of the error can be obtained, and so subdivisions proceed until the error is acceptable. In this work, 20 blocks were used. The maximum error occurs at locations on the block boundaries and is $O(E-8)$; however, most are $O(E-12)$.

Having obtained the stream function, it remains to determine the x- and y-components of the velocity. Referring to Figure 3, it is seen that ψ is computed at node points. Thus the usual expression given by $(\psi_{i,j+1}-\psi_{i,j})/0{\cdot}5(\Delta y_j+\Delta y_{j+1})$ gives the component of the velocity tangential to the top face of the cell element $\Delta x_i \Delta y_j$. However, the component of the velocity desired is perpendicular to the face of the cell element. This can be found using a four-way average of the tangential velocities obtained on boundaries of two adjacent cells. Unfortunately, this procedure does not guarantee that mass is conserved for the cell element centered on the node. This difficulty can be avoided if the values of ψ are known at the corner points of the cell element identified by the circles in Figure 3. This is the approach used here.

A biquadratic formula was used to obtain ψ at the desired corner locations by interpolating the calculated stream function between nine adjacent node points. To illustrate the procedure, consider the nine node points shown in the right-hand portion of Figure 3. Note that there is variable horizontal and vertical spacing. Also the local origin of the x- and y-co-ordinates is located at node $(i-1, j-1)$. In this way ψ within the nine-point region can be interpolated by

$$\psi=[\psi_1 N_1(x)+\psi_2 N_2(x)+\psi_3 N_3(x)]N_1(y) + [\psi_4 N_1(x)+\psi_5 N_2(x)+\psi_6 N_3(x)]N_2(y)+[\psi_7 N_1(x)+\psi_8 N_2(x)+\psi_9 N_3(x)]N_3(y), \tag{31a}$$

where

$$N_1(x)=(x-h_1)(x-h_1-h_2)/h_1(h_1+h_2), \tag{31b}$$

$$N_2(x)=-x(x-h_1-h_2)/h_1 h_2, \tag{31c}$$

$$N_3(x)=x(x-h_1)/h_2(h_1+h_2), \tag{31d}$$

and similarly for $N_1(y)$, $N_2(y)$ and $N_3(y)$. Upon rearrangement, equation (31) becomes

$$\psi=A+Bx+Cy+Dxy+Ex^2+Fy^2+Gx^2y+Hxy^2+Ix^2y^2. \tag{32}$$

The nine unknown coefficients $(A, B, \ldots, I)$ can be found in terms of the nine values of ψ at the node points $(i-1, j-1), (i, j-1), (i+1, j-1), \ldots, (i+1, j+1)$. The values of ψ at the four intersection points shown in Figure 3 are then computed from the above equation with the co-ordinates of (x, y) equal to $(x_{i-1/2}, y_{j-1/2}), (x_{i-1/2}, y_{j+1/2}), (x_{i+1/2}, y_{j-1/2})$ and $(x_{i+1/2}, y_{j+1/2})$. The required velocities are then obtained by a central difference. For example,

$$u_{i-1/2,j}=(\psi_{i-1/2,j+1/2}-\psi_{i-1/2,j-1/2})/\Delta y_j, \tag{33}$$

$$v_{i,j+1/2}=(\psi_{i-1/2,j+1/2}-\psi_{i+1/2,j+1/2})/\Delta x_i, \tag{34}$$

and so forth for $u_{i+1/2,j}$ and $v_{i,j-1/2}$. The present method retains second-order accuracy and assures mass conservation on an elemental level. It is believed to be an improvement over spatial averaging methods.

It remains to specify the wall boundary condition on the vorticity transport equation. Thus, for example, we need to evaluate terms such as

$$\left.\frac{\partial \omega}{\partial y}\right|_w=\frac{\omega_{i,j}-\omega_{i,w}}{0{\cdot}5\Delta y_j}, \tag{35}$$

where the node (i, j) is immediately adjacent to the wall, and $\omega_{i,w}$ is obtained at the wall from the

numerical analogue of equation (9). We set $\delta=\Delta x_i$ and $\varepsilon=0{\cdot}25\Delta y_j$. Then

$$u(x, \varepsilon, t)=\psi_{i,j}/0{\cdot}5\Delta y_j. \tag{36}$$

Also $\omega_{i,w}\simeq\omega(x, \varepsilon/2, t)$. The vertical velocities given by $v(x-\delta/2, \varepsilon/2, t)$ and $v(x+\delta/2, \varepsilon/2, t)$ are obtained from $-\partial\psi/\partial x$ evaluated at the designated points, where ψ is given by equation (31). The end result is

$$\omega_{i,w}=a\psi_{i-1,j}+b\psi_{i,j}+c\psi_{i+1,j}+d\psi_{i-1,j+1}+e\psi_{i,j+1}+f\psi_{i+1,j+1}, \tag{37}$$

where

$$a=-\frac{\frac{7}{2}\Delta y_j+2\Delta y_{j+1}}{(\Delta y_j+\Delta y_{j+1})(\Delta x_{i-1}+\Delta x_i)(\Delta x_{i-1}+2\Delta x_i+\Delta x_{i+1})}, \tag{37a}$$

$$b=\frac{\frac{7}{2}\Delta y_j+2\Delta y_{j+1}}{(\Delta y_j+\Delta y_{j+1})(\Delta x_{i-1}+\Delta x_i)(\Delta x_i+\Delta x_{i+1})}-\frac{8}{\Delta y_j^2}, \tag{37b}$$

$$c=-\frac{\frac{7}{2}\Delta y_j+2\Delta y_{j+1}}{(\Delta y_j+\Delta y_{j+1})(\Delta x_i+\Delta x_{i+1})(\Delta x_{i-1}+2\Delta x_i+\Delta x_{i+1})}, \tag{37c}$$

$$d=\frac{\frac{3}{2}\Delta y_j^2/(2\Delta y_j+\Delta y_{j+1})}{(\Delta y_j+\Delta y_{j+1})(\Delta x_{i-1}+\Delta x_i)(\Delta x_{i-1}+2\Delta x_i+\Delta x_{i+1})}, \tag{37d}$$

$$e=-\frac{\frac{3}{2}\Delta y_j^2/(2\Delta y_j+\Delta y_{j+1})}{(\Delta y_j+\Delta y_{j+1})(\Delta x_{i-1}+\Delta x_i)(\Delta x_i+\Delta x_{i+1})}, \tag{37e}$$

$$f=\frac{\frac{3}{2}\Delta y_j^2/(2\Delta y_j+\Delta y_{j+1})}{(\Delta y_j+\Delta y_{j+1})(\Delta x_i+\Delta x_{i+1})(\Delta x_{i-1}+2\Delta x_i+\Delta x_{i+1})}. \tag{37f}$$

For a uniform grid with $\Delta x_i=\Delta y_j=\ \ldots\ =2\Delta$ (Δ is the distance from the wall to the first node), the expression for the wall vorticity reduces to

$$\omega_{i,w}=\frac{1}{\Delta^2}\left[-\frac{11}{128}\psi_{i-1,j}+\left(\frac{11}{64}-2\right)\psi_{i,j}-\frac{11}{128}\psi_{i+1,j}+\frac{1}{128}\psi_{i-1,j+1}-\frac{1}{64}\psi_{i,j}+\frac{1}{128}\psi_{i+1,j+1}\right]. \tag{38}$$

In this form it can be seen that six values of the stream function influence the wall vorticity, but the dominant term still involves $\psi_{i,j}$. If the vertical velocity components had been neglected, only the term involving $\psi_{i,j}$ would be present, and its coefficient would be $-2/\Delta^2$, as previously noted. The use of equation (37) provides a greater coupling between the wall vorticity and the stream function than is possible with the more approximate approach. Thus it is less local in character, and this is particularly important when the streamlines have significant curvature near the wall. This occurs near stagnation and flow separation points. For this reason it is believed that the present approach for evaluating the wall vorticity represents an improvement over that normally used.

Vorticity–velocity formulation

The velocity field is governed by equations (12) and (13). The free vorticity ω is known at any time level from equation (25). The bound vorticity γ is governed by equation (16).

The non-homogeneous term in (16) involves the integral of ω over the domain. The method used to evaluate this term is the same as that used to calculate the velocity field in the fluid and will be discussed subsequently.

Points q at which values of γ are to be evaluated are directly opposite the node points of a fluid element just in contact with the step. There are 18 points on the vertical surfaces and 22 points on the top of the step.

It is assumed that γ varies linearly between surface points. Since the corner point is not explicitly included, straight-line extrapolation along the intersecting vertical and top surfaces is used to define γ at the corner. This extrapolation produces a small discontinuity there. When the linear relationships are introduced into the integrals on the left-hand sides of (16), they can be evaluated exactly in closed form. The value of ε is set equal to 10^{-6} and the values of x_p and y_p are assigned accordingly. The end result is a system of 58 non-homogeneous simultaneous equations. There is a strong diagonal dominance to the equations, the solution to which is obtained by Gaussian elimination. Having found γ, the slip velocity on the surface of the step can be obtained, as previously discussed.

The evaluation of the horizontal velocity component from equation (12) is described next. This involves integrals over the bound and free vorticity. We illustrate the procedure by considering the contributions from only a single fluid element $\Delta x_i \Delta y_j$ and a single surface element on the step, Δl_q, to the velocity at a point p in the fluid.

To a first approximation we consider that $\omega_{i,j}$ and γ_q can be treated as point vortices of strength $\omega_{i,j}\Delta x_i \Delta y_j$ and $\gamma_q \Delta l_q$. Then we have approximately

$$\Delta u_p \simeq 1 - \frac{1}{2a}[K_1(x_i, x_p, y_j, y_p) - K_1(x_i, x_p, -y_j, y_p)]\omega_{i,j}\Delta x_i \Delta y_j$$

$$-\frac{1}{2a}[K_1(x_q, x_p, y_q, y_p) - K_1(x_q, x_p, -y_q, y_p)]\gamma_q \Delta l_q . \tag{39}$$

For convenience, we define the geometrical terms by single coefficients and write simply

$$\Delta u_p \simeq 1 + CTU_{f,ij}\omega_{i,j} + CTU_{b,q}\gamma_q, \tag{40}$$

where it is recalled that the total contribution from all the spatially periodic regions is included in the above coefficients.

The point vortex approximation becomes poorer as p approaches (x_i, y_j) or (x_q, y_q). Therefore we only apply this approximation when the separation distance is greater than 100 times l, where $l = \sqrt{(\Delta x_i^2 + \Delta y_j^2)}$ or $l = \Delta l_q$. When the separation distance is less than this, we do a more exact calculation. We first subtract the contribution of the single element from the total. Let this contribution for a free-vortex element be given as

$$CAU_{f,ij} \cong -\frac{1}{2\pi}\frac{y_p - y_j}{(x_p - x_i)^2 + (y_p - y_j)^2}\Delta x_i \Delta y_j . \tag{41}$$

A similar expression can be given for $CAU_{b,q}$, except that Δl_q replaces the area of the cell element and the subscript p is replaced by q. Next we do a more exact integration over the elements in question. For a free-vortex element, $\omega_{i,j}$ is assumed to be uniform over a cell, but the co-ordinates x_i and y_j are allowed to vary over the cell. The integration can be carried out exactly and in closed form. Call this result $CEU_{f,ij}$. For the bound-vortex element the procedure is slightly more complicated, since γ_q is allowed to vary linearly between points on the surface of the step. The expression can still be obtained analytically and in closed form, but now the result involves contributions due to γ_{q-1}, γ_q and γ_{q+1}.

The results of each of these steps must now be summed. We thus have

$$\Delta u_p = 1 + CU_{f,ij}\omega_{i,j} + CU''_{b,q-1}\gamma_{q-1} + CU'_{b,q}\gamma_q + CU''_{b,q+1}\gamma_{q+1}, \tag{42}$$

where

$$CU_{f,ij}=CTU_{f,ij}+\sum_m (CEU_{f,ij}-CAU_{f,ij})_m, \tag{43}$$

$$CU'_{b,q}=CTU_{b,q}+\sum_m [(I_1+I_2+I_3)_{b,q}-CAU_{b,q}]_m, \tag{44}$$

$$CU''_{b,q-1}=-\sum_m (I_1)_{b,q}, \tag{45}$$

$$CU''_{b,q+1}=-\sum_m (I_2)_{b,q}. \tag{46}$$

The summation over m recognizes the fact that there may be more than one such element in the vicinity of p. This happens, for example, when p is near the boundary of the computational domain.

The expressions for these coefficients, including the quantities I_1, I_2 and I_3, are quite complicated and are too lengthy to give here. The pertinent results are given in Reference 10. Although this procedure for determining the coefficients is quite involved, it is believed to be extremely accurate. Furthermore, the coefficients do not change for a given numerical grid. Grid line symmetry further reduces the number of different coefficients needed. This computational overhead need be done only once and the results stored for later use. That was the procedure adopted in the present study.

The procedure just described is also used to find the slip velocity along the bottom of the groove. Values of γ are used to determine the slip velocities on the surfaces of the step, as previously explained. These slip velocities are used in the boundary conditions for the vorticity transport equation. They determine the diffusive flux of total vorticity from the solid surfaces. Accordingly, equation (25) must be modified next to solid surfaces. To illustrate this, consider the term given by (24). It must be replaced as follows:

$$\int_t^{t+\Delta t}\left[\int_{y_{j-1/2}}^{y_{j+1/2}}\left(\frac{\partial\omega}{\partial x}\right)_{x_{i+1/2}} dy\right]dt' \simeq -Re\int_{y_{j-1/2}}^{y_{j+1/2}} U_{\text{slip}}(s,t)ds, \tag{47}$$

where the order of integration has been interchanged. Similar expressions are obtained for cells in contact with horizontal surfaces. The integration of (47) is performed by approximating the variation of $U_{\text{slip}}(s, t)$ as being linear with distance s.

Attention is drawn to the fact that the right-hand side of (47) does not contain the time increment. Thus when it is used to modify equation (25) near a solid boundary, it is the only term on the right-hand side of (25), excluding $\omega^k_{i,j}$ itself, which is not multiplied by Δt. Nevertheless, the slip velocity appearing therein does implicitly depend on Δt, and this feature is discussed further in the section in which the numerical results are presented.

In principle, a numerical integration similar to that just described can be used to find the vertical velocity component. However, this is computationally time-consuming, and one is not guaranteed that mass will be conserved in the discrete field. Therefore we obtain this component directly from a mass balance. The result is either

$$v_{i,j+1/2}=v_{i,j-1/2}-\frac{\Delta y_j}{\Delta x_i}(u_{i+1/2,j}-u_{i-1/2,j}) \tag{48a}$$

or

$$v_{i,j-1/2}=v_{i,j+1/2}+\frac{\Delta y_j}{\Delta x_i}(u_{i+1/2,j}-u_{i-1/2,j}), \tag{48b}$$

depending on whether one marches, respectively, from the bottom boundary upward or from the top boundary downward. Both procedures were used in this study. To start the calculation, the velocity at a lower solid boundary point, i.e. the first term on the right-hand side of (48a), was set equal to zero, and the solution for v was marched upward. Simultaneously, the transverse velocity at the top of the computational domain, corresponding to the first term on the right-hand side of (48b), was found from (13), and the solution was marched downward. Both operations stopped when they reached the cell element in each vertical column at which the x-component of velocity was a maximum on the inflow side. The corresponding outflow velocity component in the horizontal direction was then adjusted so that it conserved mass, as dictated by (48). This procedure was found to be necessary in order to eliminate the effect of an accumulation of small errors on an already small transverse velocity.

Surface force distribution and drag coefficient

The wall shear stress and pressure are given by equations (3) and (5). The drag coefficient is given by equation (7). The evaluation of ω_w and $(\partial\omega/\partial n)_w$ is different for each formulation, as explained below.

In the vorticity–stream function approach ω_w is known directly from the numerical analogue to (9) and, as previously discussed, it involves values of the stream function at six adjacent node points in the fluid. This wall vorticity is used directly to find the wall shear stress and is used indirectly to evaluate the wall derivative of vorticity using a finite difference expression such as given by (35).

In the vorticity–velocity formulation the wall vorticity is approximated by

$$\omega_{i,w} \simeq \omega_{i,j} \pm \frac{Re\Delta l}{\Delta t} U_{slip}, \tag{49}$$

where $\Delta l = \Delta y_j/2$ or $\Delta x_i/2$, depending on the location of the wall cell. The normal derivative, on the other hand, is approximated by

$$\left.\frac{\partial\omega}{\partial n}\right|_w \simeq \pm \frac{Re}{\Delta t} U_{slip}. \tag{50}$$

The pressure contribution to the drag involves a double integration, and the viscous contribution involves a single integration. The same numerical integration procedure was used for both formulations. The pressure distribution was first found from (5). For this, the distribution of $(\partial\omega/\partial n)_w$ was approximated by piecewise linear segments between wall points, and the integration was performed to obtain values of the pressure at each wall point. The final integration of both ω_w and $(\partial\omega/\partial n)_w$ to get C_D was performed using the trapezoidal rule.

DISCUSSION OF RESULTS

The calculations begin with the impulsive acceleration of the fluid over the wall. Thus initially there is zero free vorticity everywhere and the flow field is assumed to be purely potential in nature. At this single instant only, the fluid slips tangentially over the grooved wall. The slip velocity at the wall is thus all that is needed to find the wall pressure distribution from the Bernoulli equation for steady flow, which is applicable immediately following the impulsive motion of the fluid.

The slip velocity is obtained directly for the vorticity–velocity approach, but for the vorticity–stream function approach this is calculated from the derivative of ψ evaluated at the

wall. A second-order scheme is used to approximate the stream function near the wall, after having first obtained this quantity over the whole flow field for the case $\omega = 0$.

The wall pressure distribution for potential flow at $t = 0^+$ is shown in Figure 4. In this and all subsequent figures to be presented, the triangular symbols pertain to results from the vorticity–velocity (V–V) approach and the solid lines pertain to results obtained using the vorticity–stream function (VSF) approach.

It can be seen from Figure 4 that there is almost exact congruence between the wall pressure results, except at the two corners located at $s = 2{\cdot}0$ and $s = 4{\cdot}0$. Because the slip velocity is infinite at these corners, the pressure should equal negative infinity there. In fact the pressure is not calculated exactly at these points. Rather, the calculations proceed up to the wall points which are immediately to the left of the corners by the distance 0·004467. The values of wall pressure at the corners are then obtained by linear extrapolation using the two adjacent points on the left-hand side of each corner.

Using the potential flow obtained by each method as the initial flow condition, the solutions are advanced forward in time until $t = 6{\cdot}0$ is reached. All of the results to be presented are for $Re = 100$ (based on the groove depth). The time increment used in these calculations is limited by the stability criterion imposed by the explicit Euler scheme used to obtain equation (25). This changes slightly during the course of the calculations since it involves the unknown velocities, and it must be met in each set of V–V and VSF calculations. A further limitation is implied by the use of equation (17) in the V–V formulation, and this is discussed next.

Following Lighthill[6] (see also References 9 and 10), it is reasoned that the new free vorticity produced at the wall is governed approximately by the one-dimensional unsteady diffusion equation. That is, to a first approximation the net convection in a direction parallel and transverse to the wall can be neglected compared to the transverse diffusion. Whenever a slip velocity occurs at the wall at some time t, it is presumed that new free vorticity is produced impulsively at time t^+, and this has an approximately Gaussian distribution one time increment later. It can be shown that this new vorticity is essentially confined to a layer of thickness Δ if $\Delta^2 Re/\Delta t_D \simeq 12$, where Δt_D is the diffusion time. The thickness Δ is the diffusion distance and is chosen to equal the thickness of

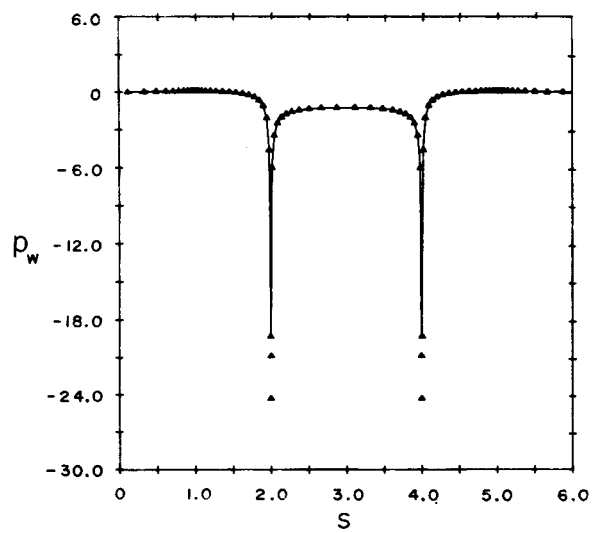

Figure 4. Wall pressure distribution obtained for potential flow at $t = 0^+$: ▲, vorticity–velocity approach; —, vorticity–stream function approach

the fluid cells immediately adjacent to the wall in the discrete field. If the transport processes were exactly one-dimensional, the slip velocity found at time t would be reduced to zero within one time increment Δt_D.

In this work $Re = 100$ and $\Delta = 0{\cdot}00893$. Thus $\Delta t_D = 0{\cdot}000665$. This cannot be regarded as a strict limit, but it does give an order of magnitude for the time increment implied in the boundary condition given by equation (17). This is because the vorticity transport near the wall is not truly one-dimensional and the convective transport is not entirely negligible.

In practice the Δt_D found in the aforementioned criterion is smaller than that dictated by the stability requirement. In this work the computational time increment ranged from 0·000956 to 0·00234. These time increments correspond to one-dimensional diffusion distances of 0·0107 and 0·0168 respectively, and these are contained within the first two spatial increments of the numerical grid (0·00893 and 0·0223 respectively).

One other feature deserves discussion, and that concerns the slip velocity calculated at the wall and used in equation (17). This quantity is greatest immediately following the impulsive acceleration of the fluid, which is taken to occur at $t = 0^+$. Except at sharp corners, where it is infinite, it can be several times the free-stream velocity. At this precise instant we envision that a vortex sheet of infinitesimal thickness exists at the surface, and immediately below it the slip velocity is reduced to zero. However, owing to the action of viscosity, this vortex sheet cannot remain infinitesimally thin, and the vorticity contained within it is redistributed in the actual flow by diffusion and convection, as explained above. Thus at the end of a time increment, i.e. $t = \Delta t$, there is generally a slip velocity at the wall, but this is typically only a few per cent of the free-stream velocity. Therefore, at $t = \Delta t^+$, new free vorticity must be produced impulsively at the wall. This forms a new vortex sheet which reduces the slip to zero at that precise instant only, but it may no longer be zero one time increment later, and so on and so forth.

It is not surprising to find that the slip velocity obtained in the sequence of calculations described above does depend implicitly on the size of the time step. Its exact dependence on Δt cannot be predicted in an unsteady simulation, but experience shows that as Δt is increased (within narrow limits consistent with the diffusion time limitation), so does the slip velocity increase. This is because the slip velocity determines the amount of total vorticity produced at the wall at the beginning of the time integration, and it is held fixed while the solution is advanced one increment in time. If Δt is increased slightly, there is a greater than expected vorticity transport by diffusion from the top of the fluid cells adjacent to the wall. This causes the vorticity in these cells to decrease slightly (in absolute magnitude). Since these cells have the greatest influence in determining the induced velocity at the wall at the end of the time increment, the absolute value of the slip velocity increases.

We now turn to a presentation of the results. Plots of the flow contours obtained by each method are shown in Figures 5–7 for representative times. The stream function contours correspond to the values 0·7, 0·3, 0·1, 0·0, −0·01, −0·02, −0·04, −0·06 and −0·08. The vorticity contours correspond to the values 1·0, 0·2, 0·0001, −0·1, −0·5, −1·0, −2·0 and −5·0. In all cases $Re = 100$.

Figure 5 shows the results at the relatively early time of $t = 0{\cdot}5$. There is almost exact congruence of the contours shown in the left- and right-hand portions of the figure. A small separation bubble has formed near the rear corner of the step and at the two corners of the groove. Flow has penetrated the groove considerably. At $t = 1{\cdot}5$ (Figure 6) the separation zone is well developed and the vorticity layer has enveloped the entire groove. At the last time for which comparisons can be made (Figure 7), the entire groove is filled with recirculating flow and there are small separation zones in the corners of the grooves. As at the earlier times, there is essentially no difference in the flow pictures obtained by the two methods.

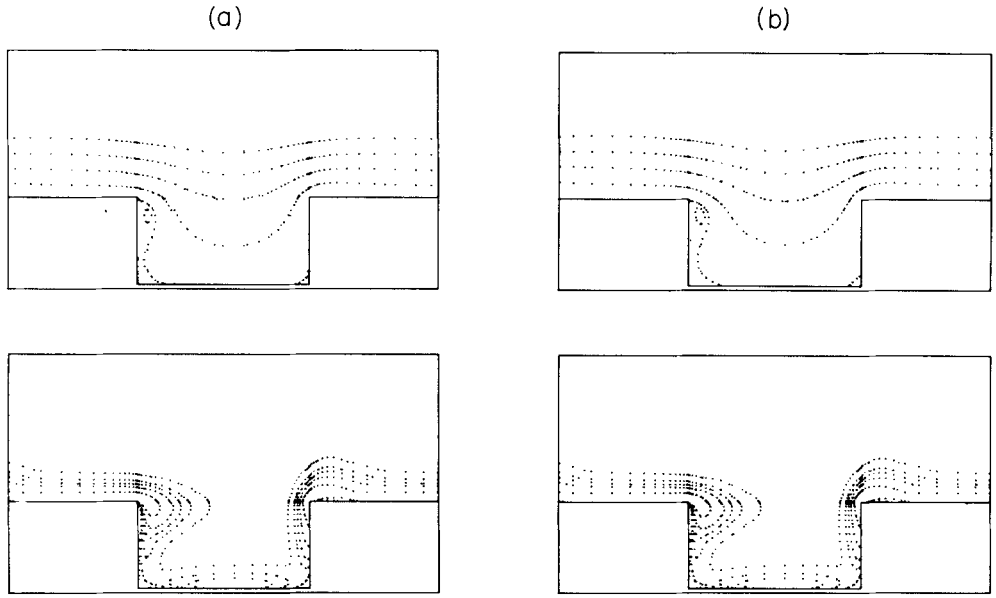

Figure 5. Stream function (top) and vorticity (bottom) contours at $t=0{\cdot}5$: (a) vorticity–velocity approach; (b) vorticity–stream function approach

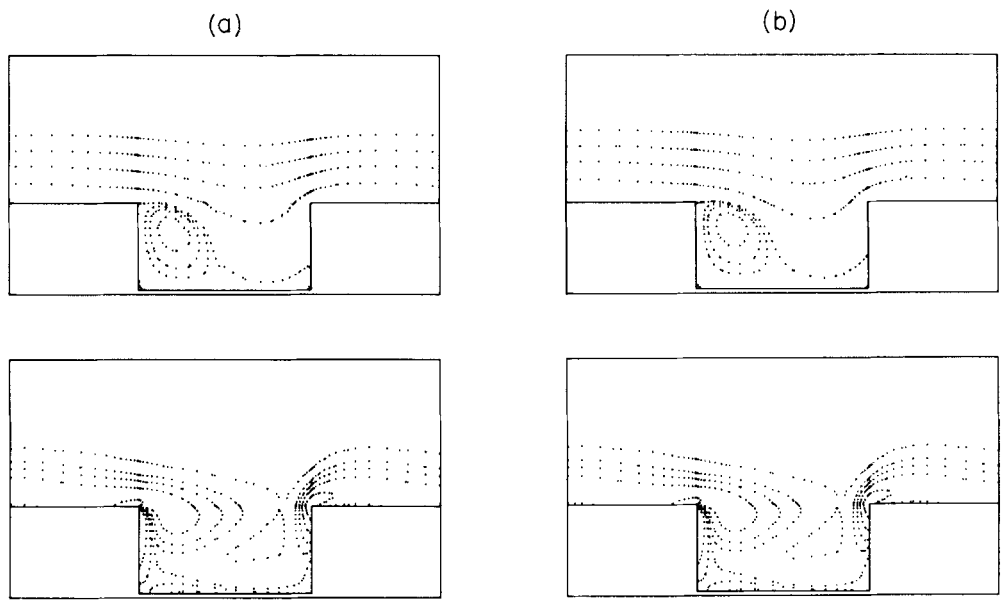

Figure 6. Stream function (top) and vorticity (bottom) contours at $t=1{\cdot}5$: (a) vorticity–velocity approach; (b) vorticity–stream function approach

Because of the close agreement between the flow patterns obtained by the two methods, it was decided to advance the solution using only the vorticity–stream function approach to the much greater time level of $t=16{\cdot}0$. The results are shown in Figure 8. As will become apparent later, this still does not represent a steady-state condition. Nevertheless, these patterns are in qualitative agreement with those obtained in Reference 17 for steady flow in a channel with one grooved wall.

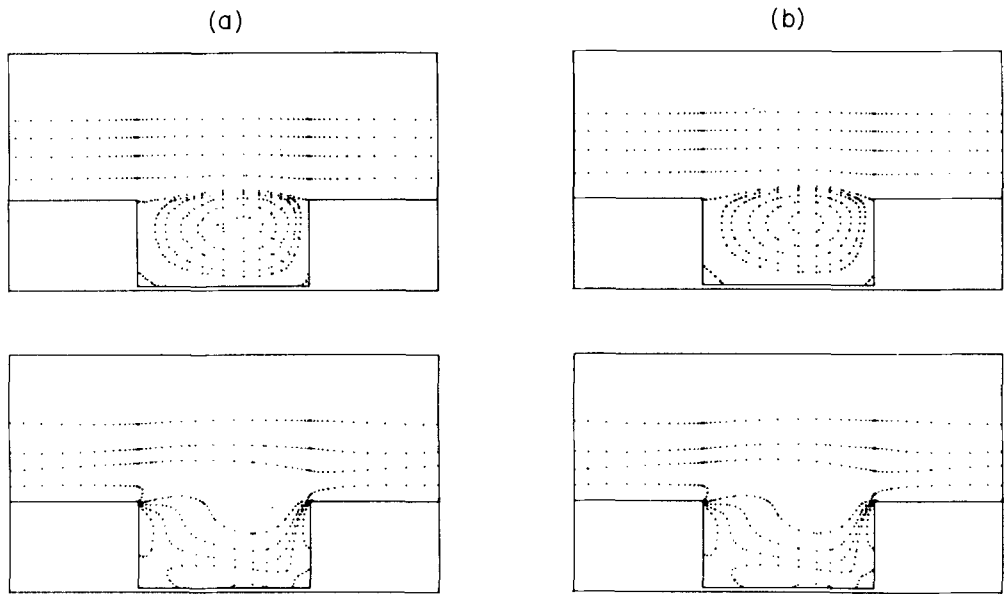

Figure 7. Stream function (top) and vorticity (bottom) contours at $t=6{\cdot}0$: (a) vorticity–velocity approach; (b) vorticity–stream function approach

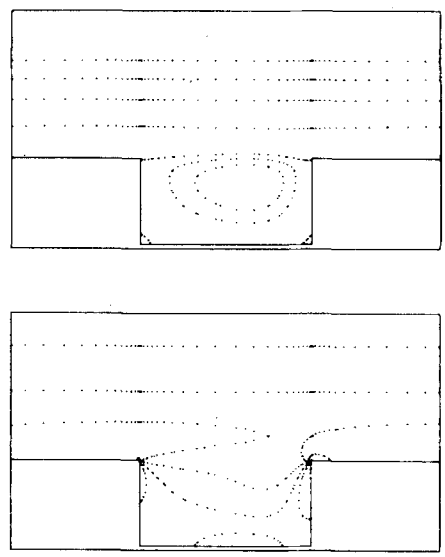

Figure 8. Stream function (top) and vorticity (bottom) contours oobtained by the vorticity–stream function approach at $t=16{\cdot}0$

A further comparison of the results is provided by examining typical velocity profiles at two representative time levels. These are shown in Figure 9. Time values of $t=0{\cdot}5$ and $6{\cdot}0$ have been chosen, and profiles of the x-component of velocity are shown for the centre of the groove, the front corner of the step, the centre of the step and the rear corner of the step. All of the velocity

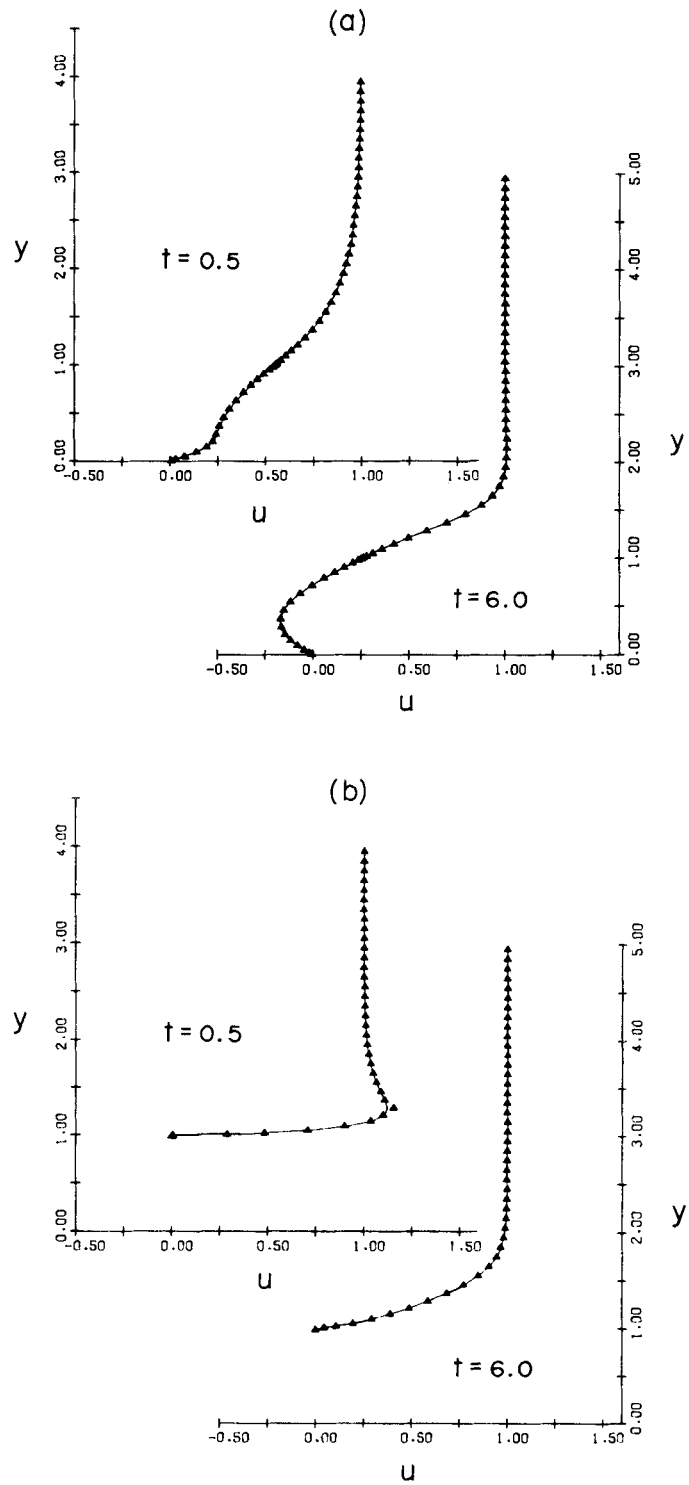

Figure 9. (a, b)

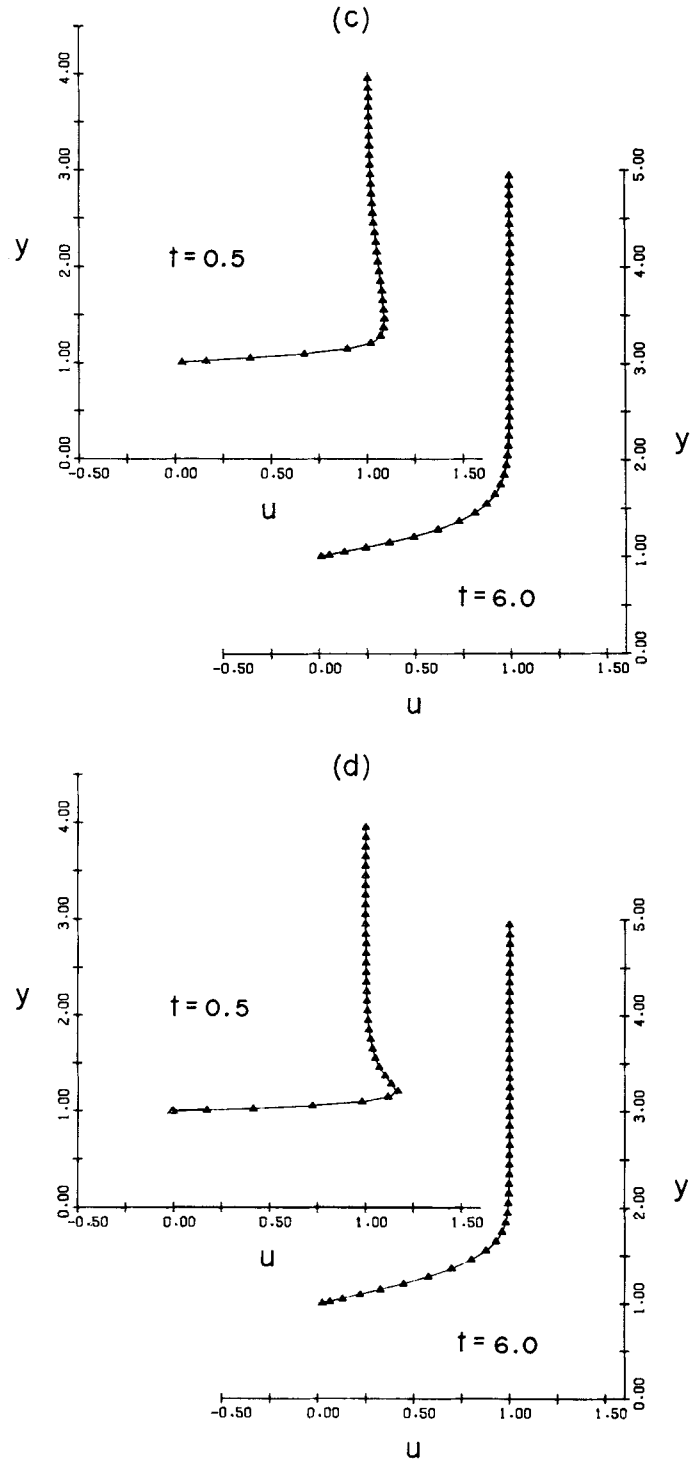

Figure 9. Comparison of velocity profiles in the x-direction: (a) $x=0$; (b) $x=1{\cdot}00$; (c) $x=2{\cdot}00$; (d) $x=3{\cdot}00$; ▲, vorticity–velocity approach; —, vorticity–stream function approach

points are shown, and it can be seen that there is good spatial resolution of the profiles, even at the sharp corners of the step at early time. There is only a slight departure between the predictions obtained by the two approaches at $t = 0{\cdot}5$ and $x = 1{\cdot}0$ and $3{\cdot}0$. This is where the profiles attain their maximum values. Otherwise the curves are essentially identical. This provides *a posteriori* evidence that the two velocity formulations yield essentially the same results. At the last time shown, the profiles along the top of the step ($x = 1{\cdot}0$, $2{\cdot}0$, $3{\cdot}0$) are smooth and regular, and they reveal a substantial viscous layer, which is to be expected at this low Reynolds number of 100.

A more discriminating test of the two methods is provided by the predictions for the wall shear stress and pressure distributions. There are shown in Figure 10 at three different time levels. In each case the distribution is shown for the developed length s along the contour of the groove and step. The same pressure scale is used in order to give a better visual sense of the changes in the pressure distributions with increasing time.

The distributions show the expected sharp peaks and valleys at the corners, which correspond to $s = 2{\cdot}0$ and $4{\cdot}0$. For $t = 0{\cdot}5$ and $1{\cdot}5$ the wall shear stress is slightly greater at the corner points for the vorticity–stream function predictions. This is not too surprising since the wall shear stress is directly related to the wall vorticity, and this is obtained directly in that approach. On the whole, the predicted wall shear stress is essentially the same for the two approaches. This is not the case, however, for the wall pressure distributions. There is close agreement up to the upstream corner of the step ($s = 2{\cdot}0$), but beyond that point there is a pronounced departure between the predictions. At the downstream point $s = 6{\cdot}0$ the pressure should return to its starting value of $0{\cdot}0$ imposed at $s = 0$. Otherwise the flow field is not spatially periodic, as stipulated in the analysis. The failure of the wall pressure distribution to return to zero after one spatial period is a major deficiency of the VSF approach. Admittedly, the situation appears to improve as time advances to $t = 6{\cdot}0$, but this is because the pressure level is decreasing overall.

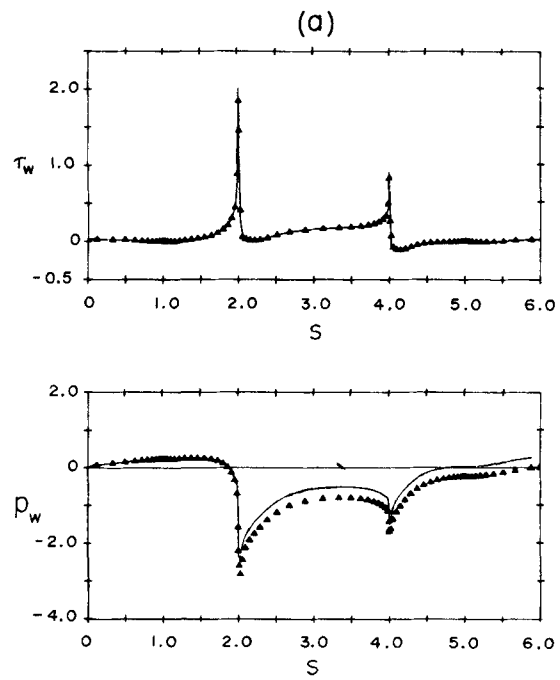

Figure 10. (a)

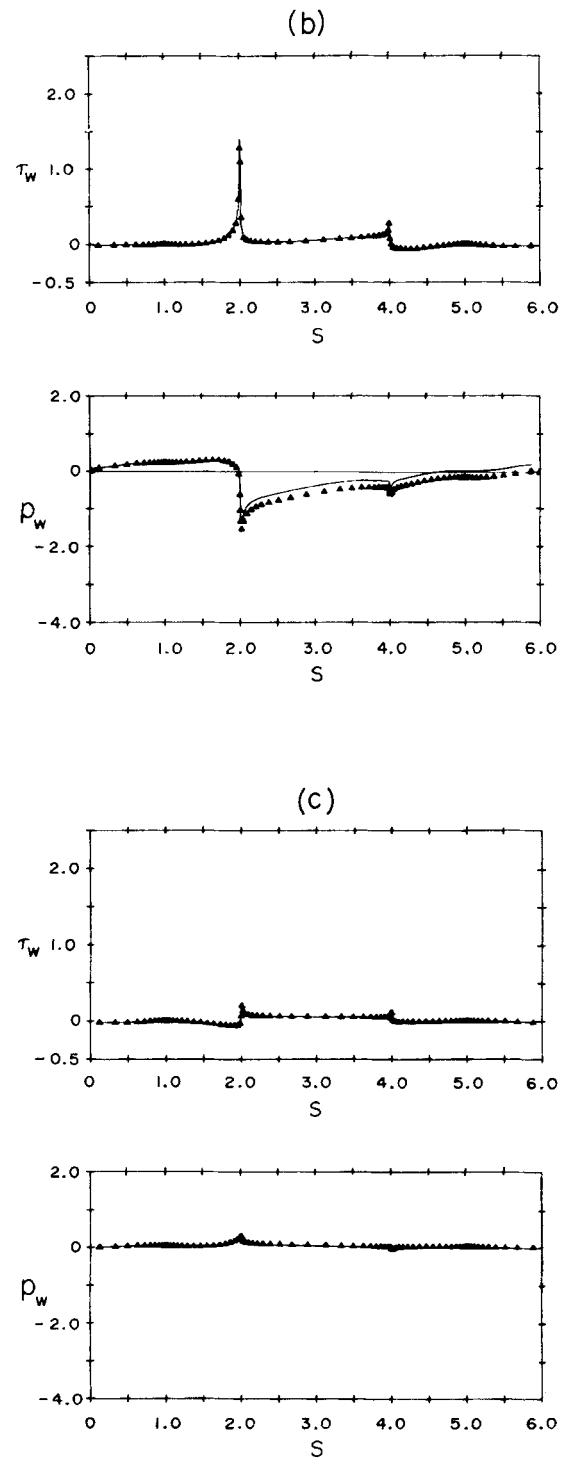

Figure 10. Comparison of the wall shear stress and pressure distributions: (a) $t = 0{\cdot}5$; (b) $t = 1{\cdot}5$; (c) $t = 6{\cdot}0$; ▲, vorticity–velocity approach; —, vorticity–stream function approach

Table I. Comparison of the predicted wall pressures at the corner points of the step and the downstream boundary of the computational domain

	$s=2{\cdot}0$		$s=4{\cdot}0$		$s-6{\cdot}0$	
t	V–V	VSF	V–V	VSF	V–V	VSF
0^+	−24·3	−19·3	−24·3	−19·3	0	0
0·5	−2.21	−1·92	−1·64	−1·35	$-0{\cdot}247\times10^{-4}$	0·276
1·0	−1·54	−1·32	−0·945	−0·724	$-0{\cdot}272\times10^{-3}$	0·221
1·5	−1·05	−0·884	−0·604	−0·426	$-0{\cdot}295\times10^{-3}$	0·181
2·0	−0·645	−0·520	−0·400	−0·260	$-0{\cdot}343\times10^{-3}$	0·143
4·0	0·267	0·278	−0·0805	−0.0680	$-0{\cdot}992\times10^{-3}$	0·0144
6·0	0·290	0·282	−0·0376	−0·0643	$-0{\cdot}262\times10^{-3}$	0·0229
16·0	—	0·106	—	−0·0738	—	0·00633

The values of the wall pressure at the corner points and $s=6{\cdot}0$ are summarized in Table I for a series of time levels. Note that the values at the corner points have been obtained by extrapolation, as described in connection with the distribution shown in Figure 4. However, the pressure is not singular at these points, as it is for potential flow. Therefore the extrapolation is reasonable.

The qualitative trends in the pressure distributions are the same for both formulations. At early times there is a depression in the wall pressure at the corner $s=2{\cdot}0$. This is because the flow is directed upward along the front vertical face and accelerates around the corner. At later times the pressure develops a local peak there as it becomes a local stagnation point for the flow. The quantitative agreement is less favourable, however. Most importantly, and as remarked earlier, the pressure at the location $s=6{\cdot}0$ is very nearly zero for the V–V approach, but is far from zero for the VSF approach. There has been no attempt to force this value to zero directly. Rather, it is an indirect result of the enforced spatial periodicity and the vorticity boundary conditions. These results demonstrate that there may be essential congruence of the flow field interior to the fluid, and yet there can be substantial departures in the predictions of the surface forces.

As would be expected, the wall pressure distributions have a significant influence on the drag predictions. Only the pressures on the front (s between 1·0 and 2·0) and on the back (s between 4·0 and 5·0) of the step enter into this portion of the drag coefficient. The wall shear stress contributes only a minor portion to the overall drag.

The drag coefficient predicted by the two approaches is shown in Figure 11 as a function of time. The departure between the predictions is substantial at early times. Between $t=4{\cdot}0$ and 5·0 the values cross over, and the drag obtained by the V–V approach converges toward zero faster than that obtained by the VSF approach. The numerical values for $t=0{\cdot}5$, 1·0, 1·5, etc. to 6·0 are, respectively, as follows: 1·043(0·781), 0·778(0·569), 0·631(0·458), 0·523(0·385), 0·376(0·307), 0·277(0·262), 0·200(0·215) and 0·151(0.175), where the values in parentheses are from the VSF approach. The smaller values of C_D from the VSF approach at early times are consistent with the higher pressures on the rear of the step, as compared with those predicted by the V–V approach.

As will become evident in the discussion to follow, the drag must asymptotically approach zero for large time. This trend is not seen in the predictions using the VSF approach. When these calculations were ceased at $t=16{\cdot}0$, $C_D=0{\cdot}115$. At $t=15{\cdot}0$ the value of C_D is 0·118. Clearly the rate of decrease is extremely slow, and it is not efficient to carry the calculations further using a time-marching method.

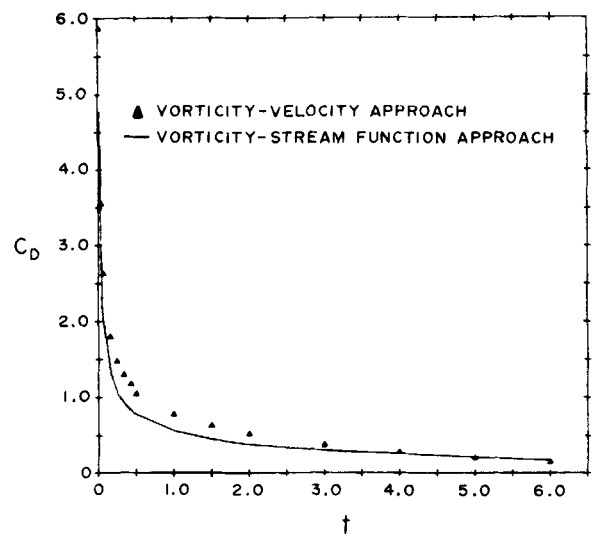

Figure 11. Variation of overall drag coefficient with time

The numerical test case used here corresponds to the Rayleigh–Stokes problem for a rough wall. The problem for a smooth wall has an analytical solution which is well known. It shows that the boundary layer grows in proportion to $(\nu t^*)^{1/2}$. The vorticity distribution is Gaussian in the variable $-y^{*2}/4\nu t^*$ and thus has zero slope at the smooth wall for $t^* > 0^+$. All of the free vorticity is produced at the instant of impulsive acceleration. The vorticity at the wall, and thus the skin friction drag, decreases towards zero in proportion to $(t^*)^{-1/2}$. It can be shown that if U is the terminal velocity of the fluid following impulsive acceleration, which is also the slip velocity at the wall for $t^* = 0^+$, then overall vorticity conservation requires that the total vorticity of the boundary layer be $-U$ for all time.

For the grooved wall studied here, there is no analytical solution, but a great deal can be reasoned about its behaviour. The imposed spatial periodicity of the pressure field requires that the net vorticity produced over one period be zero for $t > 0^+$. This follows from equation (5) for $l = 6{\cdot}0$, which is the developed surface length of the wall over one period, and for which $p_w(6{\cdot}0) = p_w(0) = 0$. Therefore all of the vorticity for this case must also be produced at the instant of impulsive acceleration. This spreads laterally by diffusion and a small amount of convection, but the total vorticity of the fluid must be fixed. Since no new total vorticity is produced at the wall, the free vorticity of the fluid must decay toward zero as the viscous layer grows infinitely thick. As a result, the fluid velocity everywhere continues to decelerate toward zero as time increases. The pressure and skin friction drag must eventually vanish as well.

The V–V formulation produces a numerical solution which has the aforementioned characteristics. The net production of total vorticity at the surface of the grooved wall is essentially zero for all $t > 0^+$. The drag also decays rapidly toward zero. These features are not evident in the solution produced by the VSF formulation.

Since the predicted velocity fields are essentially the same for each formulation, the reason for these discrepancies must be due to the different models used for the vorticity production at the wall. The V–V formulation uses a Neumann-type condition, which is the one most naturally related to the diffusive transport of total vorticity at the wall. On the other hand, the VSF formulation uses a local evaluation of the wall vorticity, and this is enforced as a Dirichlet

boundary condition. However, this result enters into the calculation only in the finite difference representation of the diffusive flux of total vorticity at the wall (see equation (35)). Therefore the evaluation of the wall vorticity is only intermediary to obtaining the relevant result. This term also enters into the evaluation of the wall pressure distribution and is believed to be the major contributing factor to the erroneous results.

As a closing note to this discussion, it is worth comparing the computational times needed to obtain the results over the time range $0{\cdot}0^+$ to 6·0. All calculations were carried out on a Control Data Corporation CYBER-175 with 60-bit arithmetic precision. The central processing time was 15·6 h for the V–V approach and 1·5 h for the VSF approach. In viewing these times, it is important to realize that they may change substantially for different operating systems and memory configurations on even the same model of computer. For the machine used, the core memory was extremely limited, and there was no virtual memory available. The geometrical coefficients used in the velocity induction-law calculations were stored in permanent disc files, and these had to be attached and read into small arrays during execution at each time level. Thus a significant amount of the central processing time for the V–V approach was devoted to input/output operations and not arithmetic operations.

It is expected that even with efficient storage and data transfer the V–V calculations will take two to three times as long to execute as those needed in the VSF approach. However, vector processing can reduce both times substantially, and therefore overall execution times are not considered to be prohibitive for either method.

CONCLUDING REMARKS

A careful formulation of two different numerical approaches has been made, and results obtained by the two methods have been compared. It is clear that the flow predictions are very nearly the same. Substantial differences occur only in the wall pressure distributions. However, these cannot be ignored if accurate predictions of drag are important. This underscores the deception that can occur if only flow patterns are compared. A careful examination must be made of the surface force distributions before firm conclusions about accuracy can be drawn.

In cases where the major contributor to drag is the viscous shear stress, the drag coefficient is expected to be very nearly the same for the two approaches. This would occur in boundary layer flows with negligible pressure gradients or flows in which the pressure is determined by the external field. This is not the case, however, when the pressure is determined by the viscous flow field and contributes the major portion to the overall drag.

The pressure gradient at the surface is directly linked to the vorticity poduction. The fact that this is found directly from the vorticity–velocity formulation suggests that the pressure gradient should be predicted more reliably by this method than by the vorticity–stream function approach. The resultant pressure distribution, which after all is obtained by a single integration, should also be more accurate.

Although not explicitly enforced in the present calculation, a feature of the velocity induction-law formulation (i.e. the use of bound vorticity on the surface) insures that the pressure field will be single-valued over the body. That is, there must be closure to the pressure distribution over the body. By this it is meant that the pressure must begin and end with the same value when a complete circuit is made around the surface of the body. In the case treated here, the body is the entire step in the upper and lower (image) planes. As shown in Reference 1, this is enforced by rendering the solution unique for the bound vorticity. Such an enforcement was not needed in the present analysis because of the antisymmetry imposed on the bound vorticity over the image of the

step. Under more general flow conditions than those encountered here, however, the bound vorticity distribution would have a complementary solution to its governing integral equation. This would produce a multiplicative constant which could be found uniquely by forcing the pressure distribution to close (i.e. be single-valued). This is equivalent to enforcing global conservation of total vorticity. It is noteworthy that even without the explicit enforcement of this condition in the present work, the pressure distribution obtained by the V–V approach has a remarkably good closure, and total vorticity is thus essentially conserved.

A check for global conservation of vorticity provides an important test for any numerical scheme. (In primitive variable formulations this can be done via the wall pressure calculation). Yet rarely is this done and the results reported. If they were, a better calibration of the methods could be made.

The use of integral vorticity boundary conditions seems to provide a natural means for enforcing global conservation of total vorticity, whether or not it is an explicit part of the boundary value formulation. This has been demonstrated in the paper by Quartapelle.[21] He shows that even a VSF formulation with newly derived integral boundary conditions for the vorticity can produce a solution which essentially conserves total vorticity. Thus it appears that it is not the use of the stream function *per se* which causes problems, but rather the form of the vorticity boundary conditions.

Even in the light of the above evidence, the relatively long execution times required by the present V–V approach and that by Quartapelle[21] will be viewed as a major shortcoming of the methods. For this reason, the authors have developed a hybrid approach which combines the best features of both formulations. The results of a recent investigation are reported in Reference 33. The bound and free vorticities still play the same fundamental roles in determining the surface production of free vorticity, just as they do in the present V–V formulation. Thus the integral Neumann type of boundary condition is retained. The velocity due to the free vorticity only is given in terms of the stream function. Boundary values on $\partial\psi/\partial n$ at the free boundaries of the domain are also enforced in integral form via the velocity induction law. Execution times are only slightly longer than needed by the VSF approach used in the present formulation. Furthermore, this study shows that the approach is applicable to multiple-body problems (i.e. non-simply connected flow domains), and this is a major attraction. It has yet to be determined whether or not Quartapelle's projection conditions[21] are valid for such domains.

ACKNOWLEDGEMENT

The authors wish to thank P. M. Gresho for helpful discussions as well as additional background material used in the revision of this paper.

REFERENCES

1. M. E. Taslim, R. B. Kinney and M. A. Paolino, 'Analysis of two-dimensional viscous flow over cylinders in unsteady motion', *AIAA J.*, **22,** 586–594 (1984).
2. H. J. Lugt and S. Ohring, 'Rotating elliptic cylinders in a viscous fluid at rest or in a parallel stream', *J. Fluid Mech.*, **79,** 127–156 (1977).
3. G. De Vahl Davis, 'Natural convection of air in a square cavity: a bench mark numerical solution', *Int. j. numer. methods fluids*, **3,** 249–264 (1983).
4. G. De Vahl Davis and I. P. Jones, 'Natural convection in a square cavity: a comparison exercise', *Int. j. numer. methods fluids*, **3,** 227–248 (1983).
5. A. Borthwick, 'Comparison between two finite-difference schemes for computing the flow around a cylinder', *Int. j. numer. methods fluids*, **6,** 275–290 (1986).
6. M. J. Lighthill, 'Introduction. Boundary layer theory', in L. Rosenhead (ed.), *Laminar Boundary Layers*, Oxford University Press, Oxford, 1963, pp. 57–60.

7. R. B. Kinney and M. A. Paolino, 'Flow transient near the leading edge of a flat plate moving through a viscous fluid', *J. Appl. Mech.*, **41**, 919–924 (1974).
8. R. A. Schmall and R. B. Kinney, 'Numerical study of unsteady viscous flow past a lifting plate', *AIAA J.*, **12**, 1566–1573 (1974).
9. R. B. Kinney and Z. M. Cielak, 'Analysis of unsteady viscous flow past an airfoil: part I—theoretical development', *AIAA J.*, **15**, 1713–1717 (1977).
10. Z. M. Cielak and R. B. Kinney, 'Analysis of unsteady viscous flow past an airfoil: part II—numerical formulation and results', *AIAA J.*, **16**, 105–110 (1978).
11. E. A. Cerutti, R. B. Kinney and M. A. Paolino, 'Numerical predictions for unsteady viscous flow past an array of cylinders', *Int. j. numer. methods fluids*, **6**, 715–731 (1986).
12. R. L. Webb and E. R. G. Eckert, 'Application of rough surfaces to heat exchanger design', *Int. J. Heat Mass Transfer*, **15**, 647–658 (1972).
13. M. J. Lewis, 'Optimising the thermohydraulic performance of rough surfaces', *Int. J. Heat Mass Transfer*, **18**, 1243–1248 (1975).
14. T. B. Gatski and C. E. Grosch, 'Embedded cavity drag in steady laminar flow', *AIAA J.*, **23**, 1028–1037 (1985).
15. S.-S. Hsieh and D.-Y. Huang, 'Numerical computation of laminar separated forced convection on surface mounted ribs', *Numer. Heat Transfer*, **12**, 335–348 (1987).
16. M. Ikegawa, 'A new finite element technique for the analysis of steady viscous flow problems', *Int. j. numer. methods eng.*, **14**, 103–113 (1979).
17. N. K. Ghaddar, K. Z. Korczak, B. B. Mikic and A. T. Patera, 'Numerical investigation of incompressible flow in grooved channels', *J. Fluid Mech.*, **163**, 99–127 (1986).
18. A. J. Chorin, 'Numerical study of slightly viscous flow', *J. Fluid Mech.*, **57**, 785–796 (1973).
19. J. C. Wu, 'Numerical boundary conditions for viscous flow problems', *AIAA J.*, **14**, 1042–1049 (1976).
20. L. Quartapelle and F. Valz-Gris, 'Projection conditions on the vorticity in viscous incompressible flows', *Int. j. numer. methods fluids*, **1**, 129–144 (1981).
21. L. Quartapelle, 'Vorticity conditioning in the computation of two-dimensional viscous flows', *J. Comput. Phys.*, **40**, 453–477 (1981).
22. L. Quartapelle and M. Napolitano, 'Methods for solving the factorized vorticity–stream function equations by finite elements', *Int. j. numer. methods fluids*, **4**, 109–125 (1984).
23. C. R. Anderson, 'Vorticity boundary conditions and boundary vorticity generation for two dimensional viscous incompressible flows', *Department of Mathematics, UCLA Computational and Applied Mathematics Report CAM-87-01*, 1987; also *J. Comput. Phys.*, in press.
24. P. K. G. Panniker and Z. Lavan, 'Flow past impulsively started bodies using Green's functions', *J. Comput. Phys.*, **18**, 46–65 (1974).
25. J. Gazdag, Y. Takao and J. Fromm, 'Rigorous numerical treatment of the no-slip condition in a vorticity formulation', *Numerical Boundary Condition Procedures, NASA Conf. Publ. 2201*, 1982, pp. 367–377.
26. P. J. Roache, *Computational Fluid Dynamics*, Hermosa Press, Albuquerque, NM. 1972.
27. L. M. Milne-Thomson, *Theoretical Hydrodynamics*, 4th edn, MacMillan, London, 1966, pp. 570–572.
28. S. C. Hung, 'The unsteady viscous flow over a grooved wall: a comparison of two numerical methods', *Ph.D. Dissertation*, University of Arizona, 1986.
29. A. C. Hindmarsh, P. M. Gresho and D. F. Griffiths, 'The stability of explicit Euler time-integration for certain finite difference approximations of the multi-dimensional advection–diffusion equation', *Int. j. numer. methods fluids*, **4**, 853–897 (1984).
30. P. M. Gresho, S. T. Chan, C. D. Upson and R. L. Lee, 'A modified finite element method for solving the time-dependent, incompressible Navier–Stokes equations. part 1: theory', *Int. j. numer. methods fluids*, **4**, 557–598 (1984).
31. P. M. Gresho, S. T. Chan, C. D. Upson and R. L. Lee, 'A modified finite element method for solving the time-dependent, incompressible Navier–Stokes equations. part 2: applications', *Int. j. numer. methods fluids*, **4**, 619–640 (1984).
32. R. V. Madala and B. E. McDonald, in D. L. Book (ed.), *Finite-Difference Techniques for Vectorized Fluid Dynamics Calculations*, Springer-Verlag, New York, 1981, ch. 7.
33. R. B. Kinney, M. E. Taslim and S. C. Hung, 'A hybrid computational approach to multiple-body viscous-flow problems: application to large-eddy breakup in a boundary layer', *J. Comput. Phys.*, in press.